공학박사 학위논문

Enhanced light extraction efficiency of OLEDs using various light extraction structures

다양한 광추출 구조를 적용하여 향상된 유기발광다이오드의 광추출효율

2018년 2월

서울대학교 대학원

재료공학부 하이브리드재료 전공

한 경 훈

Abstract

Enhanced light extraction efficiency of organic light emitting diode using various light extraction structure

Kyung-Hoon Han
Department of Materials Science and Engineering
The Graduate School
Seoul National University

Organic light-emitting diode (OLED) is promised lighting sources as lightings and display. In order for OLEDs to be utilized in the industry, the light extraction efficiency of OLEDs needs to be improved further. The light extraction structure for the display requires high light extraction efficiency improvement, low spectral change depending on the viewing angle, low pixel blur and high contrast ratio. In addition, fabrication process that does not damage the thin top electrode layer is required for top-emitting OLED (TEOLED). The light extraction structure for the lighting requires high light extraction efficiency improvement, low spectral change depending on the viewing angle, uniform emission pattern and high color quality. Bottom-emission OLED (BEOLED) are selected for lighting so, various light

extraction method can be applied. High power efficiency and color quality are required to compete with other light sources, including LEDs.

To enhance extraction efficiency, various light extraction methods have been reported such as, microlens array, photonic crystal, scattering film, corrugated device etc. Among various methods, fabrication of organic micro cone array by vacuum deposition has potential as light extraction structure for display because of damage-less fabrication method, high enhancement ratio and spectral stability. But, size of the organic structure needs to be reduced in order to meet the actual display manufacturing time. In addition, when the size of structure goes to nano, precise optical simulation is needed for calculating optimized structure. As light extraction structure for lighting vacuum nano hole array (VaNHA) has potential with electrical stability due to flat surface, high extraction efficiency in comibation with half-spherical lens. Green OLED with hexagonal VaNHA and half spherical lens was demonstrated to extract air, substrate and waveguide mode but, for uniform emission pattern, hexagonal pattern can't be applied in lighting.

This thesis concerns two research topics: (1) extraction efficiency of TEOLED with organic nano lens array (NLA) for display, and (2) extraction efficiency and color quality of OLED with VaNHA for lightings. Our analysis shows that each method could reach the proper light extraction method for display and lightings.

The paper consists of two parts as display and lighting. In **Chapter 1,** efficiency of OLED, the optical loss path, the light extraction methods, and finite difference time domain (FDTD) method are briefly reviewed.

In **Chapter 2**, we first explain the process of calculating the optical property

distribution of a top-emitting OLED with light extraction structure by FDTD method. We will discuss the computational complexity of the finite difference method, and compare it with the calculated value of the classical electromagnetic dipole model for the verification of the above calculation results. Next, the calculation results of the light extraction efficiency of the TEOLED with the hexagonal NLA are described.

In **Chapter 3**, we discuss the TEOLEDs with organic nano lens array (NLA). Oragnic NLA can be fabricatied without damage to OLED, by organic vapor phase deposition (OVPD) method. Acheivable extraction efficiency of NLA was calculated by FDTD modelling. With simulation result, optimal distribution for extraction is suggested and with high refractive index material and height of NLA, higher extraction efficiency can be achieved than efficiency with organic material (n=1.8). TEOLED with NLA showed enhanced efficiency of 50% with low pixel blur and low spectral change with viewing angle. Blue emitting TEOLED with NLA also showed enhancement ratio of 1.5 with low spectral change with viewing angle.

In **Chapter 4**, we discuss the white OLED with randomly distributed VaNHA with unprecedently high efficiency of EQE 78% and power efficiency of 164 lm/W. Random pattern consists of 3 kinds of pillars with different radius of 120, 150 190 nm. With combination of half-spherical lens, almost air, substrate and waveguide mode of light can be extracted. By mode analysis calculation, extractable light can be increased with thick distance from metal electrode and emitting dipole. By random distribution, white OLED with VaNHA showed uniform emission pattern

and spectral stability with viewing angle. FDTD calculations were performed to investigate the origin of high light extraction efficiency enhancement of Si_3N_4 and air extraction structures. The larger the difference between the refractive index of the dielectric layer and the nano hole array, the larger the light extraction efficiency.

In **Chapter 5**, we discuss the theoretically achievable color quality of white tandem devices with various light extraction structure. First, color quality according to the proportion of the emitting dyes was calculated which is ideal value whole photolumeniscent (PL) spectrum is extracted. In consideration of micro cavity, achievable color quality of device without light extraction layer, device with half spherical lens, device with high refractive index and lens, device with high refractive index substrate and lens and elongated distance with dipole and metal electrode. Simulation result is compared with experiment result and matched well. By based this model, highly efficient tandem OLED with high color temperature (> 5,000 K) can be fabricated. The WOLEDs showed maximum EQEs of 45.6 and 79.4% and maximum LE of 48.9 and 94.0 lm/W for WOLED without and with lens, respectively.

Keywords: Organic light emitting diodes, light extraction, finite difference time domain, OLED display, top-emitting OLED, OLED lightings, tandem OLED, color quality

Student Number: 2013 - 30767

Contents

List of Tables

List of Figures

Chapter 1. Introduction

1.1 Efficiency of Organic light emitting diodes

There are many ways to show the efficiency of OLEDs such as external quantum efficiency (EQE), power efficiency (PE, lm/W), current efficiency (CE, Cd/A) lumen per dollars etc. Among those values, EQE is one of the widely used assessment matrics in efficiency of light-emitting diodes. The EQE, η_{EQE}, is defined as the number of photons per injected electron;[1] i.e.,

$$\eta_{EQE} = \eta_{\text{int}} \times \eta_{out} = \gamma \times \eta_{S/T} \times q_{eff}(\phi_{PL}, \Gamma) \times \eta_{out}(\Theta, \Gamma) \qquad (1)$$

Where, η_{IQE} is internal quatum efficiency (IQE), η_{out} is out-coupling efficiency, γ is the charge balance factor, $\eta_{S/T}$ is the fraction of radiative excitons ($\eta_{S/T}$=0.25 for fluorescent emitters and $\eta_{S/T}$=1 for phosphorescent emitters), q_{eff} is the effective radiative quantum yield of the emitter in the cavity structure, ϕ_{PL} is photoluminescent quantum yield of emitting material, Γ is a factor related to device structure, Θ is farction of horizontally oriented dipoles respectively.

The IQE of OLEDs can reach 100% by exploiting various materials such as organic materials harvesting triplet excitons in the emission process,[2,3] *p*- or *n*-type dopants in the transport layers,[4,5] or charge injection layer[6] to improve the charge injection. However, η_{out} of OLEDs is limited in 20~30% (in consideration of isotropic orientation) due to waveguide and total internal refraction (TIR) which

come from the large difference in the refractive index between the organic layer and air. Therefore, out-coupling efficiency remains the biggest hurdle to improve the efficiency of OLEDs.

1.2 Optical loss modes in OLEDs

As shown in Figure 1.1, the optical modes are composed of the air mode, the substrate mode, the waveguide mode, the surface plasmon polaritons (SPPs), and the electrode absorption.[7-11] The OLEDs consist of an organic layer (n = 1.7~1.8) sandwiched between a transparent conducting oxide (TCO), such as indium tin oxide or indium zinc oxide (n = 1.9~2.1) on a glass substrate (n = 1.45~1.55), and a reflective metal electrode. Due to large refractive index difference between air and organic, significant amount of light is waveguided in the ITO-organic stack (waveguide mode). And total internal reflection occurs between the glass and the air interface, and light is transmitted back to the organic stack without being extracted. Due to the SPPs at the interface of the metal and the organic, generated light is dissipated in absorptive cathode region. A small portion of light also is absorbed at the TCO. Thus, light extraction efficiency of the OLEDs which has emitting dopoles with isotropic orientation and without light extraction layer is limited in only 20~30%.

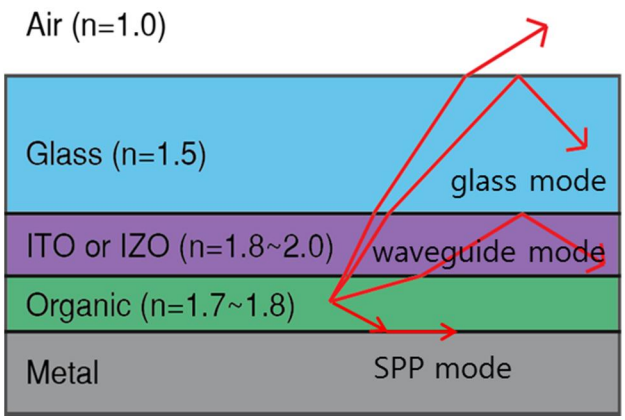

Figure 1.1 Various kinds of light out-coupling losses in normal structure OLEDs.

1.3 Light extraction methods of OLEDs

There has been tremendous light extraction methods reported. Among various classifications, position of light extraction structure is good parameter to determine. Generally, external method means light extraction structure is positioned outside substrate and internal method means light extraction layer is positioned between substrate and OLED stack.

Figure 1.2 shows typical external light extraction methods including micro lens array (MLA),[12-14] luminaire,[15] substrate with scatter,[16-20] high refractive index[21-22] and roughned surfaces.[23-24] MLA, luminaire and roughened surfaces extracts light by reducing incident angle below critical angle between air and structure. Scatter causes multiple scattering and ultimately converts the light above the critical angle into an angle within the critical angle. The external light extracting structure has advantages that it is easy to fabricate and apply, but the extractable light is limited to the substrate mode. In display, external light extraction structure generates a blurring effect on the display panel because of the presence of thick substrate.

Figure 1.3 shows typical internal light extraction methods including photonic crystal (PC),[25-28] randomly dispersed nano pillar array,[29,30] low refractive index grid,[31,32] moth eye,[33,34] nanoparticle[35] and corrugated device etc.[36-39] Nano pillar array extracts waveguide mode by giving additional momentum. Generally, periodic array (PC) extracts specific wavelength and distort the angular spectrum. For extracting broadband of light randomly dispersed pillar array is used for light

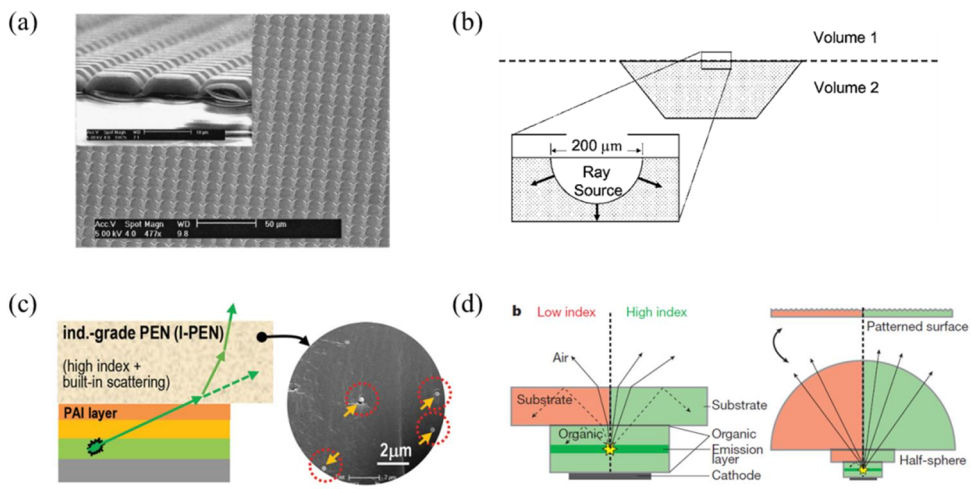

Figure 1.2 Typical external light extraction methods including (a) micro lens array (b) luminaire, (c) substrate with scatter and (d) high refractive index.

extraction. Moth eye structure extracts the light by anti-reflection effect which comes from impedance matching by graded index. The internal light extraction structure has the advantage of a potentially high extractable light, but only methods that do not adversely affect the reliability of the OLED can be used. The corrugated device extracts the SPP mode resulting to high light extraction efficiency, but non-uniform electric field is formed between the electrodes to change the electrical characteristics of the device.

Besides, device tuning without structure can be included as light extraction method. Those parameters are micro cavity effect,[40,41] orientation of emitting dipole,[42,43] low refractive index of organic material[44] and selection of alternative electrode[45,46] etc.

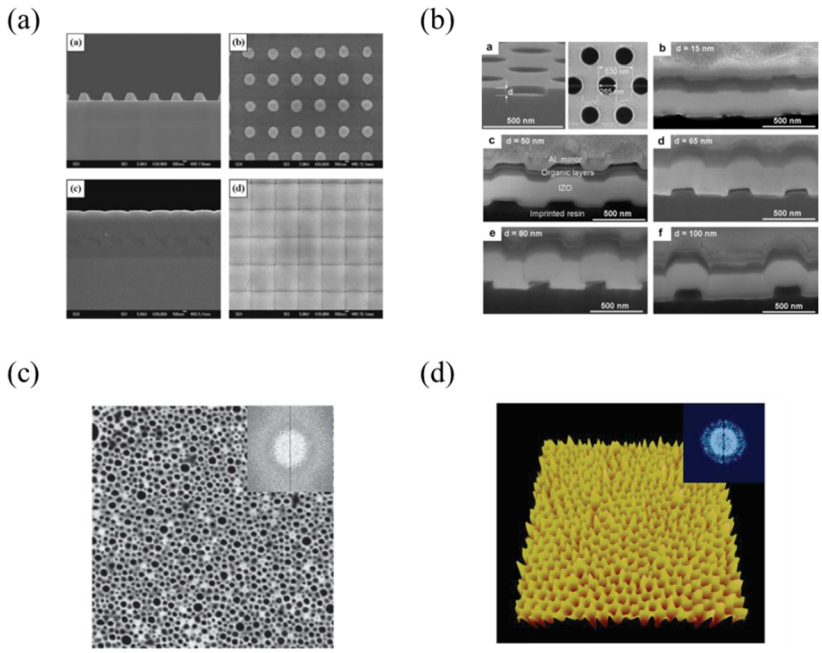

Figure 1.3 Typical internal light extraction methods including (a) photonics crystal (b) corrugated device, (c) randomly dispersed nano pillar array and (d) moth eye.

1.4 Finite difference time domain method

To reduce the burden of repetitive experiments, simulation of the proposed optical structure before the fabrication is important. Figure 1.4 shows classification of computational electromagnetics. High frequency method is used for calculation of OLED with micro structure with combination of electrical dipole model.[14,20] Light extraction efficiency of OLED with nano structure is solved only low frequency method. In computational electromagnetics, a method is rigorous if there exists resolution parameter that when taken to infinity, finds an exact solution to Maxwell's equations. Finite difference time domain (FDTD) method have advatages when compared to finite elemet method (FEM) such as no pre- of post-processing (required FEM), inclusion of nonlinearity much easier (than FEM), time-marched arrays of fields for intuitive movie generation and easy to get frequency response (FFT) etc.

The FDTD method is a numerical analysis technique used for solving Maxwell's equations in complex geometries. The time-dependent Maxwell's equations (in partial differential form) are discretized using central-difference approximations for the spatial and temporal partial derivatives. Since it is a time-domain method, FDTD simulations can cover a wide frequency range (by exploiting Fourier transform properties) with a single simulation run and handle nonlinear material properties in a natural way. In FDTD, space is discretized into box-shaped cells, which are small in comparison to the wavelength (Figure 1.5). The so-called cubic Yee cell uses the following conventions: the electric field is

defined at the edge centers of the cube;[47] the magnetic field is defined at the face centers of the cube; the electric permittivity/conductivity is defined at the cube center and the magnetic permeability/magnetic loss is defined at the cube corners.

From the Noda et al.'s calculation of mode fraction of OLED,[48] FDTD method have been utilized as optical analysis tool for FDTD method for far-field distribution,[49-50] light extraction efficiency[51-53] and transmittance of nanostructure.[54]

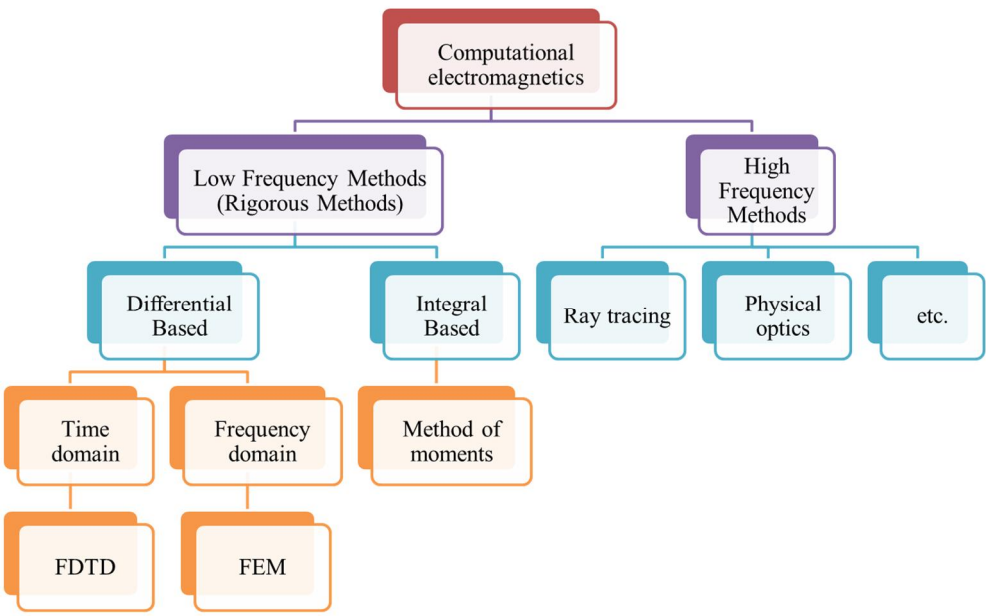

Figure 1.4 Classification of computational electromagnetics method.

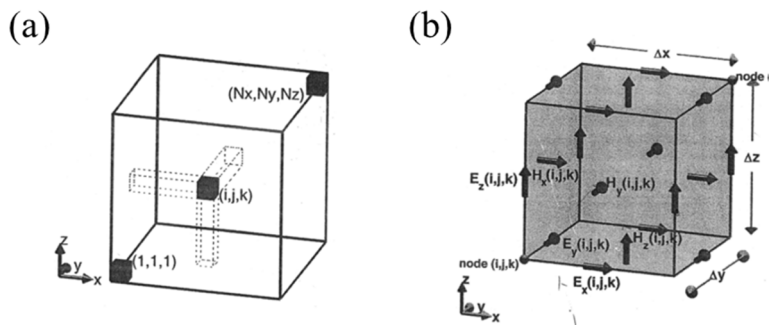

Figure 1.5 Shematic sturcture of Yee lattice in (a) FDTD simulation and (b) unit cell.

Chapter 2. Optical simulation method of light extraction in top emitting organic light emitting diode using finite difference time domain method

2.1 Introduction

Organic light emitting diodes are promised as next generation display sources for high color quality, fast response time, applicability to flexible substrate and potentially low cost. In order to commercialize OLEDs successfully, power efficiency of OLEDs needs to be improved further. Most of efficiency loss is due to low light extraction efficiency from high refractive index of emitting material. Although there have been tremendous researches for increasing light extraction efficiency,[12-39] consideration on how to apply the light extraction layer in fabrication process is insufficient. In display, top emitting OLEDs are utilized for high aperture ratio and fabrication sequence of transistor and display. For inhibiting damage to OLED stacks, only damage-less method can be selected as fabrication method of light extraction layer. Nowadays, several reports such as vacuum evaporatio,[55,56] and reflective subelectrode grid[57] have shown potential for applicability in industrial level. Especially fabrication of organic nanolens array have advantages in damage-less method, manufacturing process that does not break vacuum, large area process and low fabrication cost. As the feasibility of the light extraction structure on top-emitting device increases, the demand for an accurate

calculation of light extraction efficiency also increases.

In this report, we propose calculation method of Purcell factor which correlates totally generated power of electric dipole and light extraction efficiency of top-emitting OLED with organic nanolens array using finite difference time domain (FDTD) method. FDTD method have been utilized as calculation tool for mode fraction,[48] far-field distribution,[49,50] light extraction efficiency[51-53] and transmittance of nanostructure.[54] Calculation of TEOLEDs with nanostructure has not been reported well because of difficulty in calculation of Purcell factor. Purcell factor is affected by reflected light to emitting dipole and reflected light is complicated when the nanostructure is near dipole.[58,59] For precise calculation, position and size of the power monitors should be carefully set and the Purcell factors calculated at each position should be averaged. Commercial-grade simulator (FDTD solutions) was used to perform whole calculation.[60]

We investigate the calculation factors affecting in Purcell factor. By using optimized mesh size, Purcell factor and light extraction efficiency is calculated. For verify the modelling, light extraction efficiency and Purcell factor of TEOLED with IZO and Al are compared with results using classical electric dipole model.[61-63] TEOLEDs with organic nanolens array with hexagonal distribution and radius of 200, 300 and 400 nm and fill factor of 0.7 are utilized. From position dependent calculation, exact light extraction efficiency is calculated. Moreover, we also calculated energy loss in metal electrode and anode. We also calculated extraction efficiencies with distance from dipole to metal electrode and horizontal dipole ratio.

2.2 Methodology of optical analysis of ligh extraction

2.2.1 Simulation structure

Simulation structure is in Figure 2.1 (a). Top emitting OLEDs with IZO as top electrode is designed for calculation. TEOLED consists of Al (100 nm, n= 0.6, k=0.1), organic (160 nm, n=1.8) and IZO (60 nm, n=2.02, k=0.068). Refractive indices of organic materials are similar each other and set as 1.8. Organic layers consist of hole transporting layer (HTL, 70 nm), emitting layer (EML, 30 nm) and electron transfer layer (ETL, 20, 40, 60 and 80 nm). In order to observe the tendency according to the micro-cavities, optical calculations were carried out with different ETL thicknesses. Fill factor of organic nanolens array is 0.7 and radius are varied from 200 nm to 400 nm.

Simulation structure is 8000 * 8000 * 780 nm^3 and calculation time is 500 fs. Perfect matched layer (PML) is used as boundary condition of simulation. Other boundary method such as metal, Bloch induces artificial electric fields to dipole and results in inaccurate Purcell factor. Conductivity of PML is selected with sigma of 10 and kappa of 0.5 to avoid divergence of calculation.

The spectra used in this calculation and the signals in time domains are shown in Figure 2.1 (b). To realize green color, we set up a dipole with a wavelength of 510 nm and set the pulselength to 45 fs so that the wave packet is set close to the continuous monochromatic wave. Z direction PML was set at a distance of one

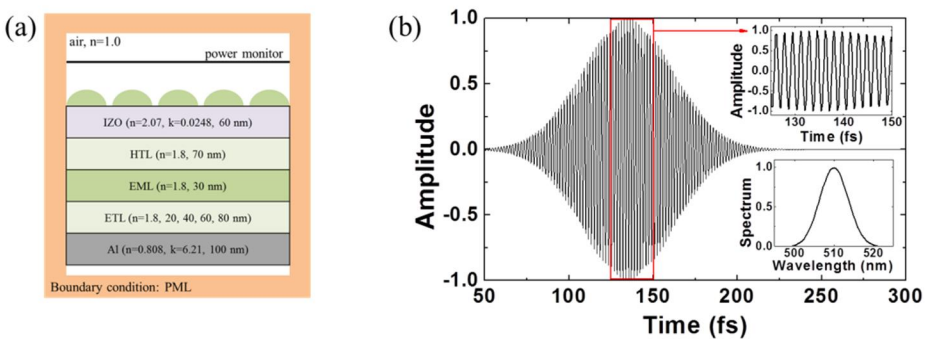

Figure 2.1 (a) Simulation structure in FDTD calculation. (b) Spectrum of dipole and time signal (inset, below).

wavelength from the IZO to prevent coupling with the evanescent field formed in the IZO-air. The power monitor is set between the PML and the IZO (or organic lens), the distance corresponding to the half wavelength.

2.2.2 Mesh size

Mesh size in finite difference method is one of the most important parameters in finite difference method (FDM). To figure out dependency of mesh size on calculation accuracy, various size of mesh is utilized. The OLED used in this calculation does not have a light extraction structure. Since the horizontal direction is symmetrical in OLED without extraction layer, mesh length in the x and y directions is set to the same size. It can be seen that the horizontal mesh length does not significantly affect the calculation results, but the calculation results vary greatly depending on the mesh length in the vertical direction only. The calculated value decreases gradually from 10 nm and converges from 3 nm. In this report, mesh size with 10 * 10 * 3 nm^3 is used for calculation time. Trade-off between accuracy and simulation time in FDM is general.

Purcell factor is changed inside cavity or resonator. In FDTD model, calculation of Purcell factor is one of the most important parameters because total emitted light in calculation is same with Purcell factor. For calculation of Purcell factor, power monitors surrounds the emitting dipole with distance. Distance of power monitors

needs to be carefully selected. When monitor is near the dipole, inaccuracy is increased. In otherwise total generated power is decreased due to absorption at metal and IZO and this absorption is not unwanted result in Purcell factor. Distance

from 3 meshes is optimized distance for calculating Purcell factor.

3.2.3 Comparison with CPS model

With these parameters, light extraction and Purcell factor of TEOLED with Al and IZO as top electrode are calculated. For verifying the model, classical electric dipole model was utilized and compare the both results. Figure 2.3 shows the extraction efficiency and Purcell factor of both device and simulation structure is in inset of Figure 2.3. Simulation results from FDTD method is matched well with result from CPS model. Dependency with orientation of dipole and thickness of ETL is also matched in FDTD simulation. This result proves the accuracy of FDTD modelling for precise calculation of Purcell factor and extraction efficiency.

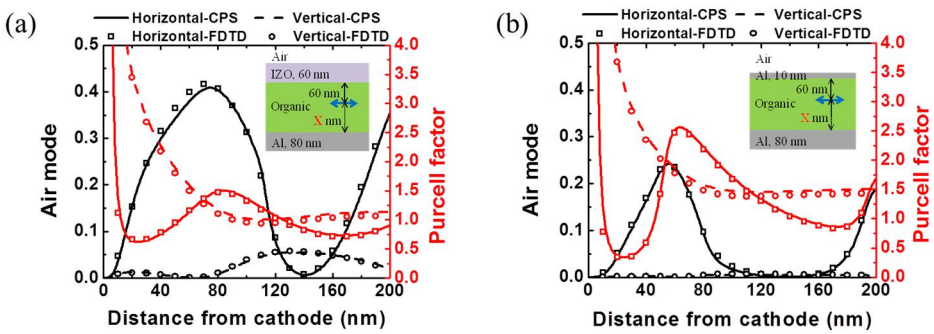

Figure 2.2 Calculated Air mode and Purcell factor of TEOLEDs with various ETL thickness. IZO of 60 nm (a) and Al of 20 nm (b) are used as top electrode of TEOLEDs. Both result is compared with results from CPS model (line).

2.3 Result and Discussion

The Purcell factor and the light extraction efficiency of the top OLED with the structure shown in Figure 2.1 (a) were calculated. The radius of the lens used is 300 nm and the fill factor is 0.7. Positions of dipoles are shown in Figure 2.3 (a). Positions are varied with 0, 0.25, 0.5, 0.75 and 1 radiuses, center of 2 lenses with x direction. Calculated Purcell factors corresponding to each position were collected together with the inset of Figure 2.3 (a). Purcell factors changed with dipole position. The Purcell factors of TEOLED with ONA varied greatly depending on the location. This large fluctuation shows that calculation of the device whose light extracting structure is close to the light emitting layer is difficult.

The extraction efficiency according to the position and orientation of the dipole is shown in Figure 2.3 (b). The light extraction efficiency is the highest at the center of the lens and gradually decreases as the distance from the center of the lens increases. Some parts are less efficient than devices without light extraction structures. In the device with the light extraction structure, the light extraction efficiencies of the dipoles in the x and y directions are different, and the difference in the end portion and the outer portion of the nano-lens increases. Vertically oriented dipoles have much lower absolute values but, enhancement ratio is high due to low light extraction efficiency of device without ONA.

For understanding the other property, absorption at metal and IZO is calculated in Figure 2.4. In the time domain calculation, we cannot obtain a result

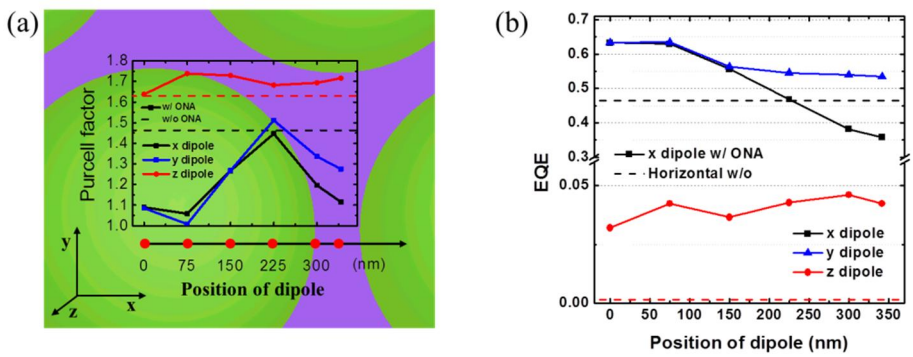

Figure 2.3 (a) Position of dipoles beneath the organic nanolens. Purcell factor with each position and orientation is in inset. (b) Calculated EQE with dipoles.

corresponding to the correct mode fraction, but we can calculate the total absorption value by setting the position of the power monitor around the material having extinction coefficient. The total amount of energy dissipated in the metal was calculated by setting the power monitor at the interface between the organic material and the metal. The energy difference between the transmitted electromagnetic wave and the reflected electromagnetic wave on the power monitor is defined as the absorbed energy by the metal. Naturally, the absorbed value had the opposite tendency to the extracted light. In vertically oriented dipoles, more than 85% of light is absorbed by the metal. Since the vertically oriented dipole has high SPP portion, the organic nano-lens array formed on the IZO does not affect the extraction.

The following equation was used to calculate the total amount of energy absorbed in IZO.[64]

$$A_{IZO}(\vec{r}, t_s) = \omega \times \mathrm{Im}[\varepsilon_{IZO}] \times |E_{IZO}(\vec{r}, t_s)|^2 \qquad (2)$$

To calculate the energy absorbed by the IZO, a 3-d power monitor of the same size as the entire IZO region was set. The amount of absorption in the horizontally oriented dipole was more than that in the vertically oriented dipole.

The light extraction efficiencies were calculated when the fill factor of the nanolens array was fixed at 0.7 and radius of lens was varied with 100, 200, 300, 400 and 500 nm. Interestingly, the tendency of extraction efficiency according to dipole location varied significantly with the radius of nanolens. The larger the radius of the nano-lens array, the higher the extraction efficiency at the center of

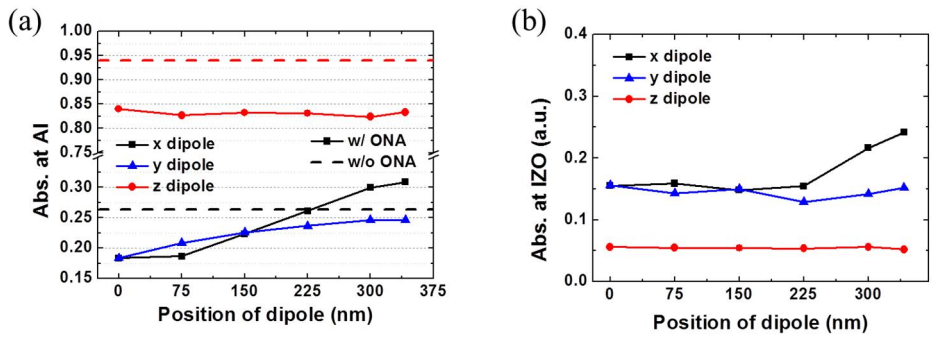

Figure 2.4 Calculated absorption at metal (a) and IZO (b) with dipole orientation and position.

the lens, but the more the extraction efficiency decreases as the distance from the center of the lens increases. When the radius is 300 nm, the difference according to the direction of the horizontal orientation dipole is largest. Since the space of organic lens is a sub-wavelength region, it is not significantly influenced by the direction of the dipole in radius 100 and 200 nm. Light extraction efficiency of TEOLED with radius of 100 nm is lower than that of the device without ONA. In the vertically oriented dipoles, the radii of the nanolens did not make a large difference.

Enhancement ratio of horizontally oriented dipole ratio is calculated in Figure 2.5. Enhancement ratio is increased with vertical dipole but, overall extraction efficiency is high with full horizontal layer. The light extraction efficiency of the device using the 400 nm radius is the highest. Since the calculation results are obtained when the fill factor is fixed, this calculation value cannot be regarded as the maximum improvement of the light extraction method using ONA. This result shows that the size of the nanostructure greatly affects the light extraction efficiency and the size control is important in the application of the upper light emitting OLED.

The structure of the nanolens was fixed at a radius of 200 nm and a fill factor of 0.7, and the light extraction efficiencies are calculated by changing the thickness of the ETL (Figure 2.6). For comparison, the mode fraction of a device without a light extraction structure was calculated using the CPS model. Device without and with

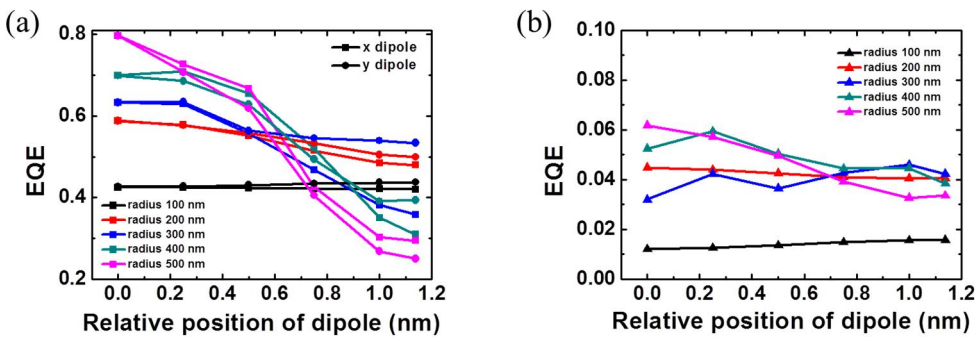

Figure 2.5 Calculated EQEs with relative positions of horizontally (a) and vertically (b) oriented dipoles with various radius of ONA.

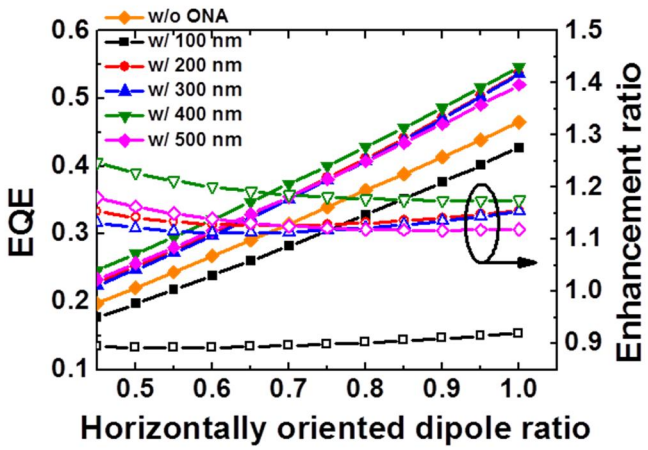

Figure 2.6 Total EQEs and enhancement ratio of TEOLEDs with ONA at various radius depending on the horizontally oriented dipole ratio.

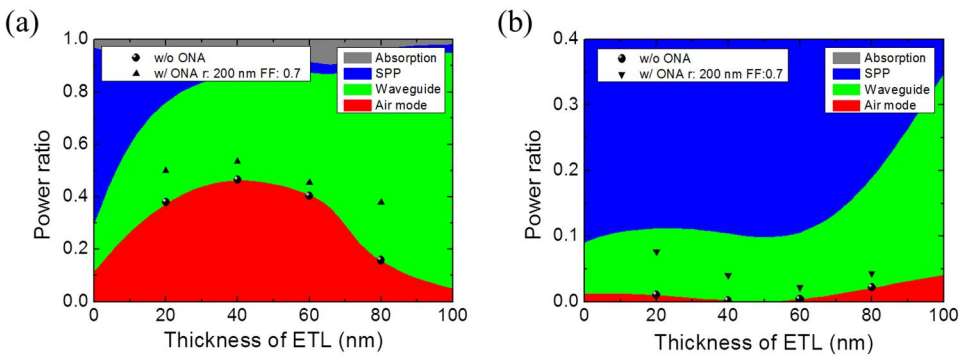

Figure 2.7 Extraction efficiencies of TEOLED without and with ONA depending on ETL thickness. Horizontal (a) and vertical (b) dipoles are calculated separately.

ONA have the highest extraction efficiency at ETL of 40 nm. The enhancement ratio of extraction efficiency of devices using thin ETL (30 nm) is higher. If the ETL is too thick, the ratio of the light traveling in the horizontal direction of the device increases, which is not very advantageous for light extraction. The light extraction efficiency of the vertical dipole of the device with ETL thickness of 60, 80 nm is similar to that before light extraction.

2.4 Conclusion

Simulation parameter is carefully selected for calculation of extraction efficiency and Purcell factor. With those parameters, result from FDTD model is matched well with result using CPS model. Dipole position is critical parameters in TEOLED with light extraction structure. Purcell factor is also changed much with dipole positions. Light extraction efficiency is high at center of nanolens and decreased with distance from center of dipole. Total enhancement ratio is only 20% which is calculated with radius of 400 nm. Absorption at bottom metal electrode and IZO layer is calculated and tendency of both are matched with tendency of extraction efficiency. From this modelling, TEOLED with extraction layer of nanosize can be calculated.

Chapter 3. Enhanced light extraction efficiency of top-emitting organic light emitting diode by using nano lens array fabricated by organic vapor phase deposition method

3.1 Introduction

A lens array containing multiple lenses with a lens diameter of <1 mm has been used as an optical functional film (a layer having functions of light extraction, refraction or scattering et al.) working in lights in a particular range of wavelength. The lenses have curved surface such as a hemisphere to act on the light. Size control is an essential technology because any kind of light can be selected by controlling the diameter. To fabricate the lens array, other technology such as a mask, a surface treatment and a molding has been combined with a deposition process,[55,56] because all deposition apparatuses have been designed to manufacture films with even surface. This results in the complicated and difficult fabrication of the lens array. A light extraction layer of organic light emitting diodes (OLEDs) can be one of the great applications of the lens array, since OLEDs have become dominant in small sized displays and are increasingly used in the production of large sized TVs and solid stated lightings. Improving efficiency has always been an important issue in OLEDs to reduce power consumption in all of these applications.

Light extraction is one of the most important technologies for improving the efficiency of OLEDs, because 60~80% of the generated light is trapped in the OLEDs as the substrate confined mode, the waveguided mode and the surface plasmon polariton mode, if there are no extraction films. Large number of methods integrating either an internal or external light extraction layer or combining both have been developed to enhance the light extraction efficiency to demonstrate high external quantum efficiency.[12-39] Despite such development, light extraction technologies are still not used for display applications because of the image blurring issues for bottom emission OLEDs used for TVs coming from thick substrate on the one hand, and difficulties of integration of the extraction methods to the completed OLEDs in top-emitting OLEDs (TOLEDs) used for small size displays on the other hand. The image blurring issue must also be considered in TOLEDs even though it is less serious, because thin layers (an encapsulation layer and a micro lens array) in the order of a few micrometers are applied on the top electrode in the TOLEDs used for small sized displays.[65] Most of the light extraction layers fabricated by wet processing are not compatible with the current TOLED manufacturing process. Furthermore, the pixel size of active matrix OLED (AMOLED) displays for mobile devices is continuously decreasing following the increase in an image resolution. Thus, the NLA with sufficiently smaller size (<1 um) is necessary to avoid the image quality degradation. The development of a deposition process for creating the NLA without combining the additional technique and compatible with the current OLED fabrication technologies is one of the greatest advances in low cost, short tact time and high resolution display

applications. In this work, we report an organic NLA fabricated using an organic vapor phase deposition (OVPD) without combining that. Formation mechanism of the NLA is investigated by using a grazing-incidence small-angle Xray scattering (GI-SAXS) analysis. To elucidate the efficacy of the NLA, optical simulations are performed. OLEDs without and with the NLAs are fabricated and characterized.

3.2 Optical simulation

The Lumerical finite difference time domain (FDTD) solutions package was utilized as the simulation program.[60] The size of the computational domain and the unit mesh was $10 \times 10 \times 0.67\ \mu m^3$ and $10 \times 10 \times 2\ nm^3$, respectively (Figure 3.1). A perfectly matched layer (PML) was used as the boundary condition. A single electric dipole was utilized as the light source which had a peak of 510 nm and a full width at half maximum of 38 nm, and was positioned at the center of the simulation structure. The calculations were carried out until 0.1% of the total power was left in the calculation domain.

The simulation results are summarized in Table 3.1. Use of NLA 1 and NLA 2 increased the light output efficiency by a factor of 1.02 and 1.48, respectively. The ~1.5-fold change in the NLA 2 based device is believed to be due to the reduction of the guided modes by scattering at the NLA pattern, which also leads to a decrease in the absorption loss at the interface between the metal and organic layers. However, the light output ratio in the NLA 1 simulation is scarcely changed, which is believed to be due to the small size of the NLA which does not scatter the light efficiently.

Without the NLA, a strong evanescent field is present at the IZO-Air interface due to the large difference in refractive indices between IZO (2.05) and air (1.0). The electric field intensity abruptly decreases from the IZO-Air interface to the air

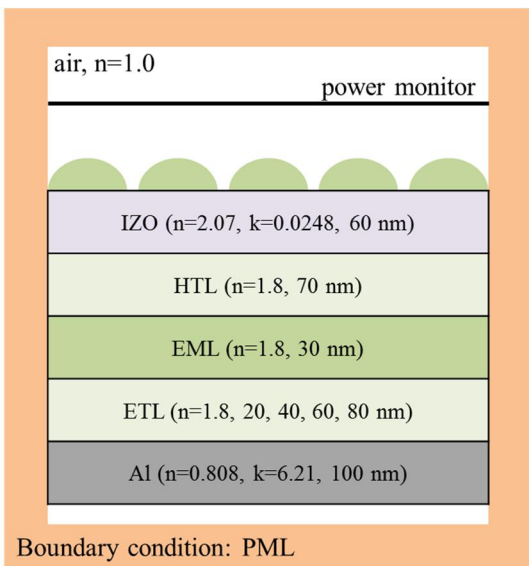

Figure 3.1 TEOLED with organic NLA in FDTD calculation.

Table 3.1 Summary of the simulation results of the mode fraction using the FDTD method for different device structures.

Structure	Extracted		Wave-guided	Absorption by metal
	fraction	Enhancement ratio	fraction	fraction
w/o	0.304	-	0.271	0.425
w/ NLA1	0.311	1.02	0.261	0.428
w/ NLA2	0.451	1.48	0.183	0.366

region. However, with the NLA, the electric field intensity is significantly reduced in the whole device, most greatly reduced at the IZO-NLA interface (ie, IZO-Air interface without NLA), and shows much slower decrease from the IZO-NLA interface to the NLA region. This indicates that the NLA extracts light otherwise trapped in the device[66,67] by mainly reducing the waveguide loss. Higher refractive index of the NLA provides lower electric field intensity at the IZO-NLA interface. This suggests that the light extraction efficiency can be further increased by using a higher refractive index material for NLA, corresponding to the results shown in Figure 3.2 (a). NPB with a refractive index of 1.8 is used for the NLA in the device fabrication, hence it is predicted that the efficiency is increased approximately 1.52 times by NLA integration in the experiments.

The total amount of energy absorbed in the Al and the IZO electrodes is calculated.[64] The absorption loss is decreased by introducing the NLA and by increasing its refractive index (Figure 3.2 (b)). The integration of the NLA with a refractive index of 1.8 (NPB) provides the larger decrease ratio of absorption at the IZO compared to that at the Al (0.13 vs 0.09).

Interestingly, even though the differences in refractive indices between NLA (1.8-2.1) and air are similar to that between IZO (2.05) and air, the electric field intensities at the NLA-Air interface are half of that at the IZO-Air interface. In addition, the electric field curves at the NLA-Air interface are very smooth. Moreover, there is a significantly slower intensity decrease from the NLA-Air interface to the air region (with NLA), compared from the IZO-Air interface to the

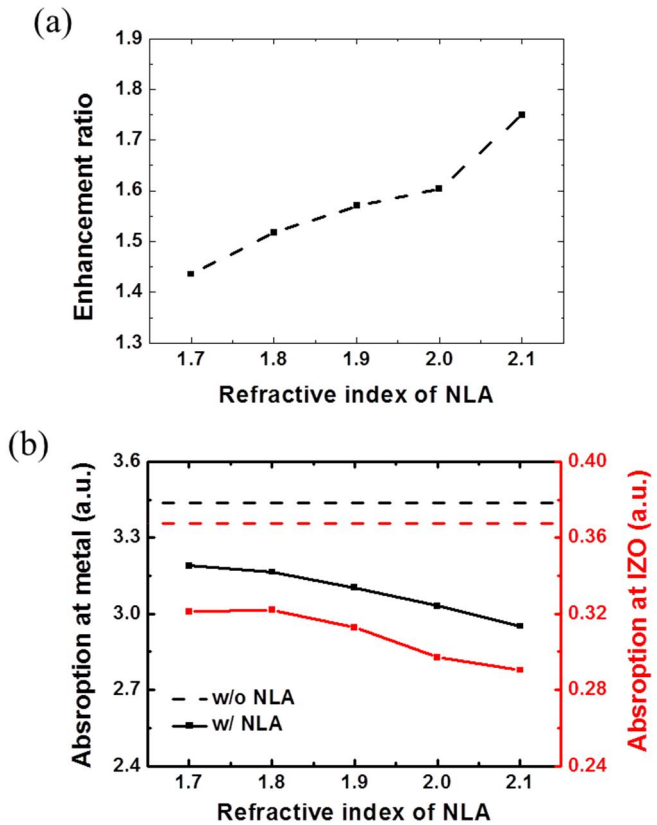

Figure 3.2 (a) Enhancement ratios of light extraction efficiency, and (b) absorptions at Al and IZO without and with NLAs with various refractive indices of NLA.

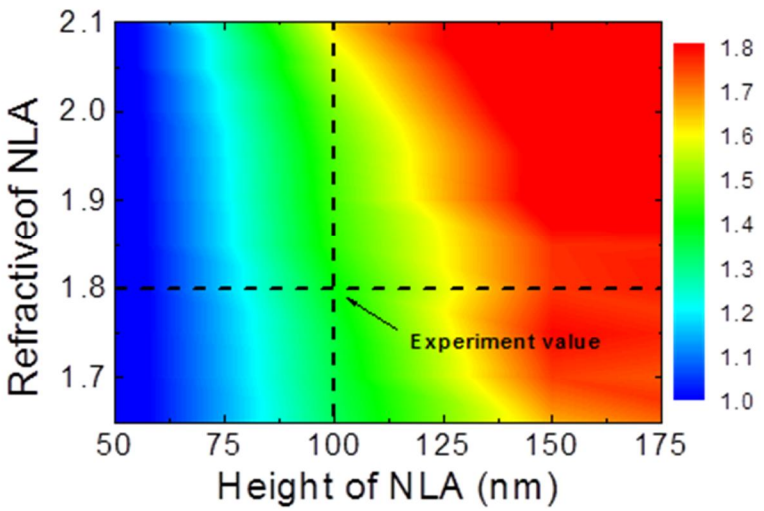

Figure 3.3 Contour plot of enhancement ratio of light extraction efficiency with fucntion of height and refractive index of NLA. Dotted line is plotted for experiment value.

air (without NLA). Therefore, we believe that the NLA efficiently sends the light out to the air, as an optically excellent scattering structure.

It has been reported that scattering layers based on 240 nm size nanoparticles fabricated by using solution processes enhance the efficiency and improve the color stability of bottom-emitting white OLEDs.[67,68] The nanoparticle process is not compatible with the processes in the current OLED industry, because it uses a wet method. The nanoparticles are internal scattering layers, as they are located between the substrate and the bottom electrode. NLA in this study is an external scattering layer because it is formed on the top electrode. To experimentally demonstrate the effectiveness of the NLA on the blue OLEDs, devices are fabricated and measured.

3.3 Experiment

3.3.1 Fabrication of NLA

The NLA was fabricated on indium zinc oxide (IZO) film using the OVPD. Neither a lithography, a shadow mask, a surface treatment, nor a molding was combined with the OVPD process. N,N'-Di(1-naphthyl)-N,N'-diphenyl-(1,1'-biphenyl)-4,4'-diamine (NPB, purity >99.9 %) powders were put into a vaporizer and then heated to generate organic vapors. The vapors were transferred by means of a nitrogen gas and deposited on the specimens (Figure 3.4). Prior to the deposition, the samples were transferred to main chamber with a base pressure of $<10^{-2}$ Torr, via a load-lock chamber. The nitrogen gas flow rate was 100 sccm. The NLA was grown at a growth rate of ~25 nm/min. The substrate temperature was -10°C.

3.3.2 Fabrication and evaluaition of green TEOLED

The inverted TOLED devices were fabricated on glass-substrates pre-patterned with a 70 nm thick indium tin oxide. The cathode and the organic layers were deposited using thermal evaporation processes at a pressure of $3x10^{-7}$ Torr. The device structure was: aluminium (Al, 70 nm) / 7wt% Rb_2CO_3 doped B3PYMPM (40 nm) / B3PYMPM:TCTA:$Ir(ppy)_2$acac (0.46:0.46:0.08 wt%, 30 nm)

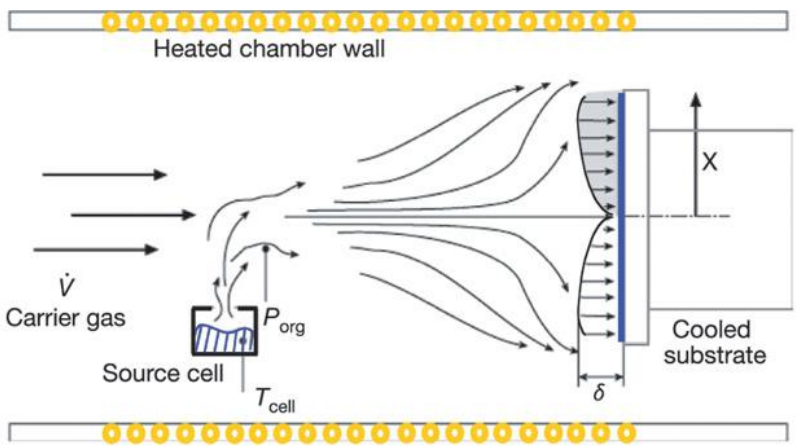

Figure 3.4 Schematic description of OVPD process.

/ TCTA (10 nm) / TAPC (10 nm) / 10wt% ReO_3 doped TAPC (40 nm) /HATCN (40 nm), where B3PYMPM, TCTA, $Ir(ppy)_2acac$, TAPC, and HATCN represent bis-4,6-(3,5-di-3pyridylphenyl)-2-methylpyrimidine, 4,4',4"-tris(carbazol-9-yl)tripheny lamine, bis(2-phenylpyridyl) iridium(iii) acetylacetonate, 1,1-bis-(4-bis(4-methyl-phenyl)-aminophenyl)-cyclohexane, and 1,4,5,8,9,11-hexaazatriphenylene hexacar bonitrile, respectively. The IZO was sputter deposited on the HATCN film by using facing targets at room temperature. The NLA was fabricated on the IZO by using the OVPD (Figure 3.5). The J-VL characteristics were measured using a Keithley 2400 programmable source meter. The angular distribution of the electroluminescence intensity was measured using the Keithley 2400 programmable source meter, a rotation stage and an Ocean Optics S2000 fiber optic spectrometer.

3.3.3 Fabrication and evaluaition of blue TEOLED

Blue fluorescent OLEDs with an inverted top emitting structure were fabricated on glass/indium tin oxide (ITO, 70 nm) substrates. Following the aluminium (Al, 70 nm) cathode deposition, organic layers composed of 1 wt% Rb_2CO_3 doped B3PYMPM (40 nm) / B3PYMPM (10 nm) / B3PYMPM:mCP:10 wt% TBPe (30 nm) / mCP (10 nm) / 10 wt% ReO_3 doped mCP (10 nm) / HATCN (50 nm) were formed using thermal evaporation processes without breaking the vacuum, where mCP is abbreviated forms of N,N'-dicarbazolyl-3,5-benzene.

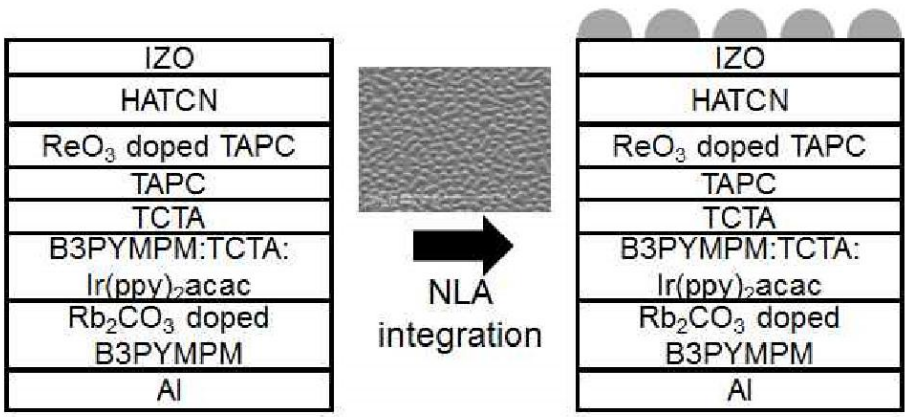

Figure 3.5 Schematic diagrams of the inverted TOLEDs before and after the NLA integration.

3.4 Result and discussion

To fabricate the NLA, the OVPD was introduced, because it enables an accurate control over the transport rates of the precursors by separately controlling carrier gas flows and the temperature of each source.[69-71] NPB was chosen as the lens material, since it has a refractive index close to that of IZO, the transparent top electrode used for this study. The OVPD is a dry process so that it is fully compatible with current fabrication processes of OLEDs.

Scanning electron microscope (SEM) images of the NLAs fabricated on the IZO layers using the OVPD are shown in Figure 3.6. When thermal evaporation process was used to fabricate the NPB film, we did not get the NLA but a planar thin film. Figs. 1a and 1b show that hemispherical nano lenses with a diameter of ~80 nm (NLA pattern 1) were formed, and some of them were impinged as indicated by arrows.

By controlling the fabrication process including the vaporizer pressure, nano lenses with a diameter of 200-700 nm (NLA pattern 2) could be fabricated as presented in Figure 3.1 (c) and 3.1 (d), indicating that the diameter is controllable by controlling process parameters. The coverage ratio of nano lens to total surface is ~70%. These morphologies indicate that islands nucleate at isolated areas and grow larger to impinge with other islands.[72]

The NLA 2 with a larger lens size has a greater tendency of the coalescence of the nano lenses, compared to the NLA 1 with a smaller lens size. Results of Figure 3.5 demonstrate that the size controllable NLA technology is developed using only

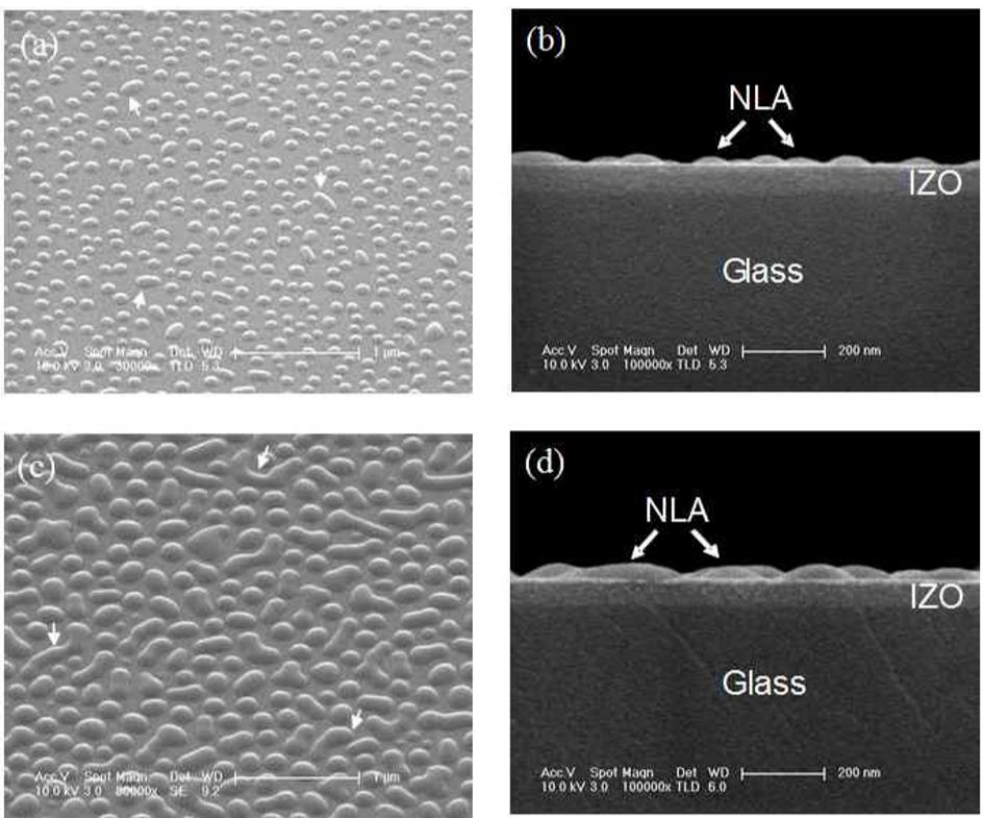

Figure 3.6 Planar (a, c) and cross sectional (b, d) SEM images of NLA 1 (a, b) and NLA 2 (c, d), respectively, showing the creation of the nano lenses on the IZO layer by using the OVPD process. The arrows (a, c) indicate the impingement of the nano lenses.

the OVPD. The size control is an important technique, because any kind of light can be chosen by adjusting the diameter.

The NLA with the diameter of several hundred nanometers (NLA 2) was easily integrated in the OLEDs by directly forming the NLA on the IZO top electrode. Figure 3.7 (a) presents the current density-voltage-luminous (J-V-L) plots of the devices without and with the NLAs. The J-V curves of the elements are similar and the turn-on voltages are the same as 2.4 V, indicating that the OVPD process does not damage the device. The element with the NLA clearly shows a higher luminance than that without NLA. Figure 3.7 (b) displays that the current efficiencies of OLEDs without and with the NLAs are 79 and 123 cd/A, at 0.1 mA/cm^2, respectively, showing an increment ratio of 1.55 by employing the NLA. The increased ratio is similar to that in the simulation results, indicating that the NLA is an optically effective scattering medium for OLEDs. Compared to the element without NLA, that with the NLA shows less photo image blurring and higher slope variation with the distance from the OLED center (Figure 3.8), indicating that the NLA provides less image blurring and increases color stability. Both devices without and with the NLAs show extremely small variation of color coordinates ($\Delta u'v'$: ~0.002) as the viewing angle changes from 0° to 60°, which is due to the adoption of the IZO top electrode.[55] The simulations using the NLA 1 are also confirmed by device data showing 1.03 times increase of the current efficiencies by the NLA 1 integration.

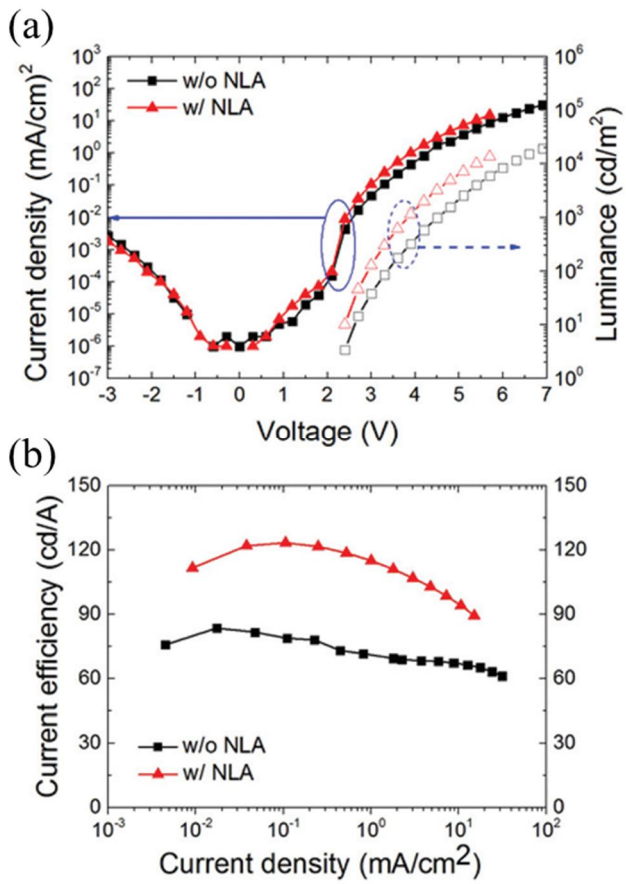

Figure 3.7 (a) The J-V-L curves, (b) the current efficiencies of the devices, showing ~1.5 times enhancement of efficiency by the integration.

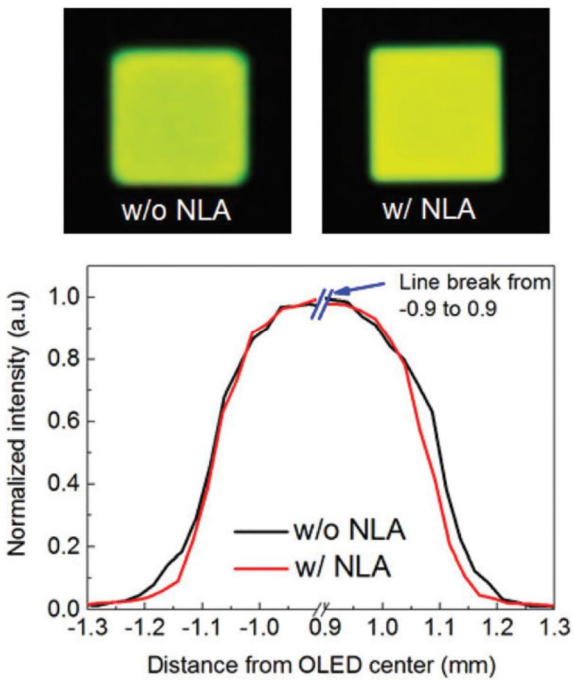

Figure 3.8 TEOLED without and with ONA. Less image blurring after integration.

Figure 3.9 (a) shows the J-V-L characteristics of the blue TOLEDs without and with the NLAs. The two J-V curves are nearly overlap, and the voltage at a current density of 10^{-2} mA/cm^2 is equal in both cases (5.5V). This indicates that the NLA process does not damage the device at all. The L-V curves display that the device with the NLA has a higher luminance at the same voltage compared to that of the device without the NLA, hence the NLA is an excellent external extraction layer that decreases the waveguide loss, as expected by the simulations. Figure 3.9 (b) illustrates that, at 1 mA/cm^2, current efficiencies of the TOLEDs without and with the NLAs are 4.6 and 7.3 cd/A, respectively. Their power efficiencies are 1.7 and 2.6 lm/W, respectively. This indicates that the NLA integration increases the light extraction efficiency by approximately 1.55 times, which agrees with the value obtained by simulations.

Figure 3.10 shows the anular spectrum of TEOLEDs without and with NLAs. The first main EL intensity peaks (at a wavelength of 462 nm) of the TOLEDs do not change between 0° and 60° regardless of the presence of the NLA. As predicted by calculations that the NLA is an efficient light scattering layer, the second main peaks (at a wavelength of 493 nm) of the element with the NLA are scarcely changed between 0° and 30°, and vary less between 0° and 60°, compared to those without the NLA. This agrees well with the results from color coordinate change measurements, $\Delta u'v'$ between viewing angles 0° and 60° (without NLA: 0.20; with NLA: 0.15). As the relative ratio of the second pick

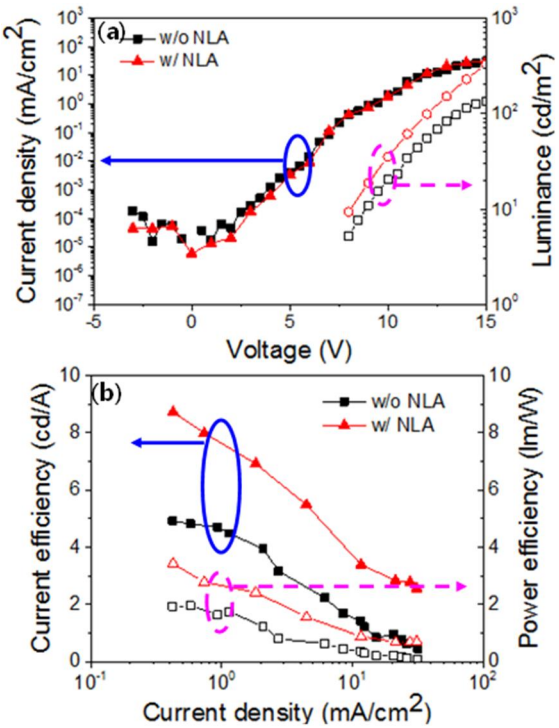

Figure 3.9 (a) The *J-V-L*, (b) current and power efficiencies of blue TOLEDs without and with NLAs.

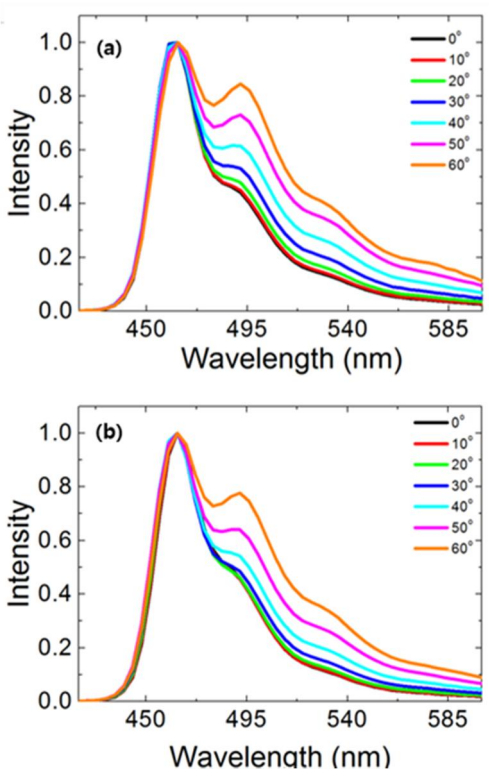

Figure 3.10 Angular spectrum data of blue TOLEDs (a) without and (b) with NLAs.

increases at a viewing angle of more than 40°, it can be seen that the NLA (NPB) does not completely mitigate the micro cavity of the TEOLED.

3.5 Conclusion

In conclusion, this work reports the diameter controllable NLA technology developed using a conventional deposition (OVPD). Formation mechanism of the NLA is interpreted and the NLA formation is reproducible in experiments in which the crystallization of organic molecules occurs.

Targeting the light extraction layer of OLEDs, the NLA with the diameter of several hundred nanometers were fabricated by controlling the process parameters. The NLA solves the issues of the non-compatibility and the image blurring. The NLA increases the light extraction efficiency by a factor of ~1.5, corresponding the number to simulation results. Thus, the NLA is an optically effective scattering medium for OLEDs. Therefore, the NLA technology opens the potential for low cost mass production of highly efficient and color stable OLEDs

Chapter 4. Theoretically achievable light extraction efficiency of white organic light emitting diode with vacuum nano-hole array

4.1 Introduction

Lighting technologies are responsible for 17% of global electricity consumption, with over 90% consumed by conventional lighting sources such as incandescent lamps, compact fluorescent lamps, and fluorescent tubes. However, the efficiencies of these conventional lighting sources are already limited (~17 lm W^{-1} for incandescent lamps and ~90 lm W^{-1} for fluorescent tube) by fundamental factors. Therefore, the solid-state lighting sources with high efficiency, such as light-emitting diodes (LEDs) and organic LEDs (OLEDs), are emerging as alternative lighting sources for the reduction of energy consumption as well as carbon emission. White OLEDs (WOLEDs) are considered as more attractive lighting sources than LEDs in terms of the quality of light, mechanical and design flexibility, free of blue hazard, and so on. However, WOLEDs with high luminous efficacy (LE) overcoming LEDs at high luminance are believed to be a distant goal at present even with large advances in light extraction during the last couple of decades.[12-42] Those advances include scatter, low refractive index layer, micro lens

array, photonic crystal, low/high refractive index grid, high refractive index substrate, corrugated structure, graded index, randomly distributed pillar array, bio mimetic structure, plasmonic nanocavity and so on. Among the proposed methods, the insertion of extraction medium between the glass and the ITO electrode is regarded to have potential for further efficiency enhancement by extracting the waveguide mode in combination with the extraction method at the glass-air interface. However, despite the efficiency improvement due to the extraction layer, many of these methods often have limitations such as diffraction pattern and color distortion to be applied to general illumination systems and high performance electronic devices. To solve these problems adderessing the angular dependence and diffraction pattern, a random pattern is introduced, but the currently reported random patterns are obtained by using spontaneous methods which have difficulty in quantitative control of randomness and poor reproducibility. It would also be recommended that the internal extraction stucture does not distort the planar structure in OLEDs to prevent the potential degradation issue coming from the rough structure because active layers of OLEDs are very thin.

Here, we report novel WOLEDs approaching the theoretical limit by using the highly effective extraction layer based on a randomly dispersed vacuum nano-hole array (VaNHA). The random VaNHA pattern was designed with random number generation function in the unit cell of 10×10 μm^2 to show no specific symmetry in the reciprocal space. The random VaNHA WOLEDs in combination with a half spherical lens exhibited comparable performance with LED lighting with

unprecedentedly high LE of 164 lm W^{-1}, originating from high maximum EQEs 78 and low efficiency roll-off. In addition, the WOLEDs showed uniform emission of high quality light with high correlated color temperature (CCT) of 3400 K, high color rendering index (CRI) around 80, no color variation with viewing angle. The light extraction structure does not have any addition detrimental effect on the device stability manifested by no electrical variation compared to device without light extraction layer.

4.2 Experiment

VaNHA fabrication: An 800-nm-thick Si_3N_4 film was deposited onto a silicon substrate using plasma-enhanced chemical vapor deposition; then, a random hole array was patterned near the surface of the silicon nitride layer using conventional photolithography and dry etching. The patterned Si_3N_4 on the silicon substrate was bonded with the glass wafer in a vacuum using the anodic bonding procedure; the bonded wafers were then dipped in a KOH solution to dissolve the silicon substrate. The fabrication process is schematically represented in Figure 4.1.

Device fabrication and evaluation: The OLEDs were fabricated on clean glass substrates or VaNHA embedded glass substrates pre-patterned with 70-nm-thick ITO under a pressure of 5×10^{-7} Torr using thermal evaporation without breaking the vacuum. The device and substrate area is 10×10 and 25×25 mm^2, respectively. Current density-voltage-luminance characteristics and EL spectra were measured using a Keithley 2400 programmable source meter and a SpectraScan PR650 (Photo Research). The EQEs of the WOLEDs w/o extraction layer were measured using Keithley 2400 programmable source meter, rotation stage and Ocean Optics S2000 fiber optic spectrometer. The Enhancement ratios of EQE and LE of WOLEDs with VaNHA were measured with an integrating sphere and a monochromator attached photomultiplier tube (PMT) as an optical detector system. A hemisphere lens with a diameter of 10 mm is attached on the glass surface with

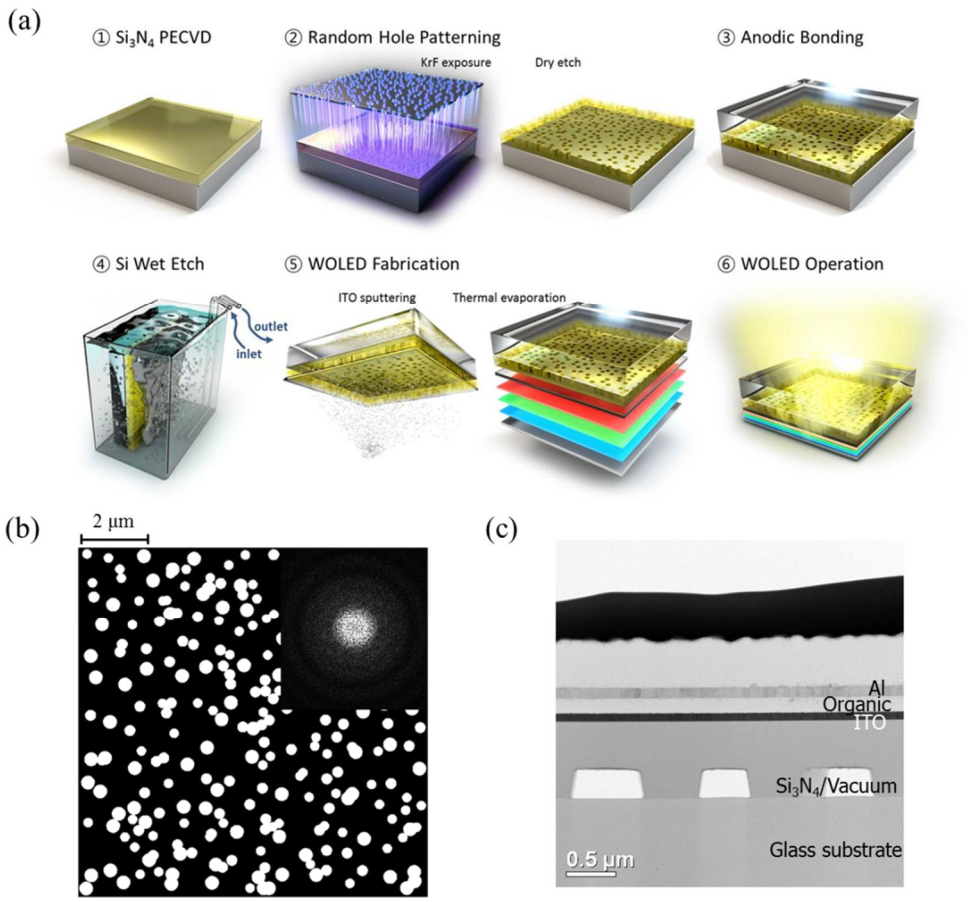

Figure 4.1 (a) Fabrication scheme of VaNHA substrate by robust reverse transfer process. (b) Designed pattern image of random distribution in 10^2 μm^2 and 2D-FFT image of the random pattern (inset). (c) Cross sectional scanning transmission electron microscopy (STEM) image of WOLED w/ the VaNHA substrate.

index matching oil.

Optical simulation (Mode analysis): The classical dipole model was used to simulate the fraction of different optical modes. This model is based on the classical electromagnetic theory with full vectorial scheme, where a molecular excited state is treated as an oscillating dipole. Mode analysis was performed under the assumption that the recombination zone is located in the middle of the emitting layer. The influence of the dopant on the refractive index of the emitting layer was ignored because of the low doping concentration.

FDTD analysis (propagation of wave): Simulation structure is shown in Figure 4.2 (a). Red, green and blue dipoles are located in the middle of emitting layers and randomly distributed within a unit cell with the dimension of 10 ×10 um^2. Spectra of dipoles are in Figure 4.2 (b). The number of dipoles were set considering the orientation of emitting dipoles and the doping concentration as follows; 252 (red, horizontal), 55 (red, vertical), 104 (green, horizontal), 29 (green, vertical), 54 (blue, horizontal) and 17 (blue, vertical)). Mesh size is used as 20×20×2 nm^3 (final dimension is for the vertical direction of OLED stack). Field propagation is captured at the center of simulation structure after 100 fs. Perfect metal (horizontal) and PML (vertical) boundary conditions were used for the calculation.[52] Simulation code for FDTD solutions is attached in Appendix.

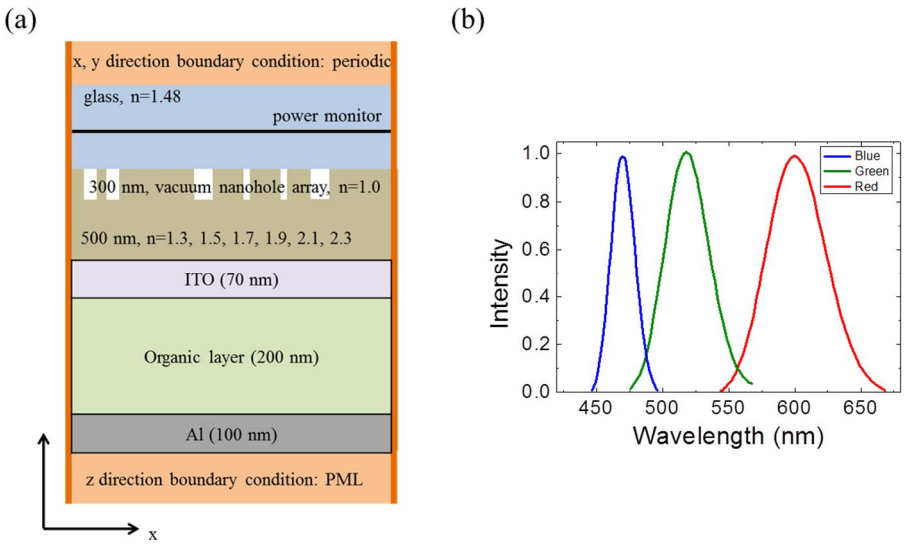

Figure 4.2 (a) Simulation structure in FDTD calculation and (b) Spectra of red, green and blue dipole used in FDTD simulation.

4.3 Result and discussion

Design of and fabrication of VaNHA and OLEDs

High quality white light sources require no color variation with viewing angle and the Lambertain intensity distribution. To obtain isotropic emission profile, a randomly dispersed VaNHA was designed in this work for the first time.

Figure 4.1 (b) displays the image of the designed random pattern. The coordinates of the holes were generated using a random number generation function, and the holes having the three different diameters were placed at the corresponding positions. By dispersing the position of holes, the randomness of vacuum nanoholes was controlled not to show any symmetric emission patterns in the unit cell of 10×10 μm^2. The hole diameters were 220, 260 and 320 nm corresponding to the half of the red, green and blue wavelength, respectively, so that the average periodicity of the aperiodic array distributes in the range of visible wavelength for efficient interaction with broadband visible light. The two-dimensional Fast Fourier Transformation (2D FFT) image of the pattern (inset of Figure 4.1 (b)) proves that the random array have no specific symmetry in the reciprocal space, expecting to have little color variation with the change of the viewing angle and the wavelength.

The designed random pattern in Figure 4.1 (b) was transferred using conventional photolithography to a Si_3N_4 layer deposited on Si wafer followed by

dry etching to form the random VaNHA in the Si_3N_4 layer. The unit cells with the dimension of 10×10 μm^2 were repeatedly arranged over 100×100 mm^2 in the photomask. The VaNHA pattern was fabricated on a 8 inch silicon wafer which promises large area production. The anodic bonding of the patterened Si_3N_4 layer with glass substrate at a high temperature (350°C) in vaccuum followed by the etching of Si substrate in a KOH solution completed the fabrication of the random VaNHA embedded Si_3N_4 layer on glass substrate. The cross sectional image of the structure is shown in Figure 4.1 (c). The surface of the random VaNHA embedded Si_3N_4 layer is flat to warrant no detrimental effect originating from the rough surface usually observed in internal light extraction structures.

Figure 4.3 schematically presents the device structure with the material, thickness and energy levels of each layer. $Ir(mphmq)_2(tmd)$, $Ir(ppy)_2(tmd)$, FIrpic were used as the red, green and blue emitting phosphorescent dyes, where $Ir(mphmq)_2(tmd)$, $Ir(ppy)_2(tmd)$ and FIrpic represent Iridium(III)bis(4-methyl-2-(3,5-dimethylphenyl)quinolinato-N,C2') tetramethylheptadionate, Iridium(III) bis(2-phenylquinoline) tetramethyheptadionate and Iridium(III) bis((4,6-di-fluorophenyl)-pyridinato-N,C'), respectively.[73] The red and green dyes have the high horizontal emitting dipole ratios (Θ) of 82 and 78%, respectively, and FIrpic also has preferred horizontal emitting dipoles with Θ of 76%.[74-76] The PL quantum yield of FIrpic, $Ir(ppy)_2$tmd and $Ir(mphmq)_2(tmd)$ are 97, 96 and 96%, respectively. The high horizontal emitting dipole ratios combined with the high PL quantum yields of the dyes will lead to high outcoupling efficiency of the device. In order to

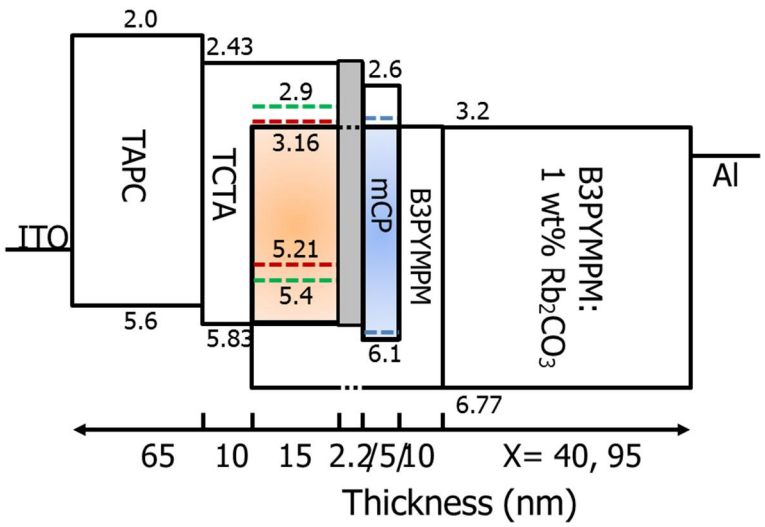

Figure 4.3 (a) Schematic diagram of OLED structure with energy levels. Hollow boxes represent the LUMO (upper line) and HOMO (under line) levels of the materials. The orange and blue shaded boxes represent the HOMO and LUMO levels of the exciplex-forming co-hosts of the orange and blue EMLs, respectively. The gray shaded box represents the energy level of the buffer layer (BL). The red, green, blue, and black dashed lines show the energy levels of $Ir(mphmq)_2(tmd)$, $Ir(ppy)_2(tmd)$, FIrpic, and B3PYMPM, respectively. The bottom line and numbers represent the thicknesses of the layers.

minimize the voltage drop, 1 wt.% of rubidium carbonate (Rb_2CO_3) was used as electron dopant in the electron transport layer (ETL, B3PYMPM).

Efficiency of WOLEDs with VaNHA

The result of the mode analysis of the WOLEDs using a classical dipole model with various ETL thicknesses (0 ~ 150 nm) is shown in Figure 4.4 (a).[1] The concentrations of the red, green and blue dyes were set as 0.6:0.26:014 in the calculations. The air mode oscillates with increasing the thickness of the ETL. However, the extractable mode (summation of the air mode, substrate mode and waveguide mode) is monotonically increased with the ETL thickness. The EQE of an WOLED with ideal internal and external extraction structures can reach over 80% if the thickness of the ETL is over 150 nm. This value can be achieved without any extraction of the SPP mode which requires a rough metal surface possessing potentially detrimental effect on the device lifetime. Contour plots of EQE and extractable mode (summation of air, substrate and waveguide mode) as functions of the ETL and the HTL thickness are displayed in Figure 4.5 (a) and 4.5 (b), respectively.

Two different WOLEDs with the ETL thicknesses of 50 and 105 nm were fabricated (WOLED I and II, respectively) and compared with the theoretical analysis. The current density–voltage–luminous exitance (*J–V–L*) characteristics of WOLED II are shown in Figure 4.4 (b). Device chracteristics of WOLED I are in Figure 4.6. In lighting, total amount of emitted light is more important than light

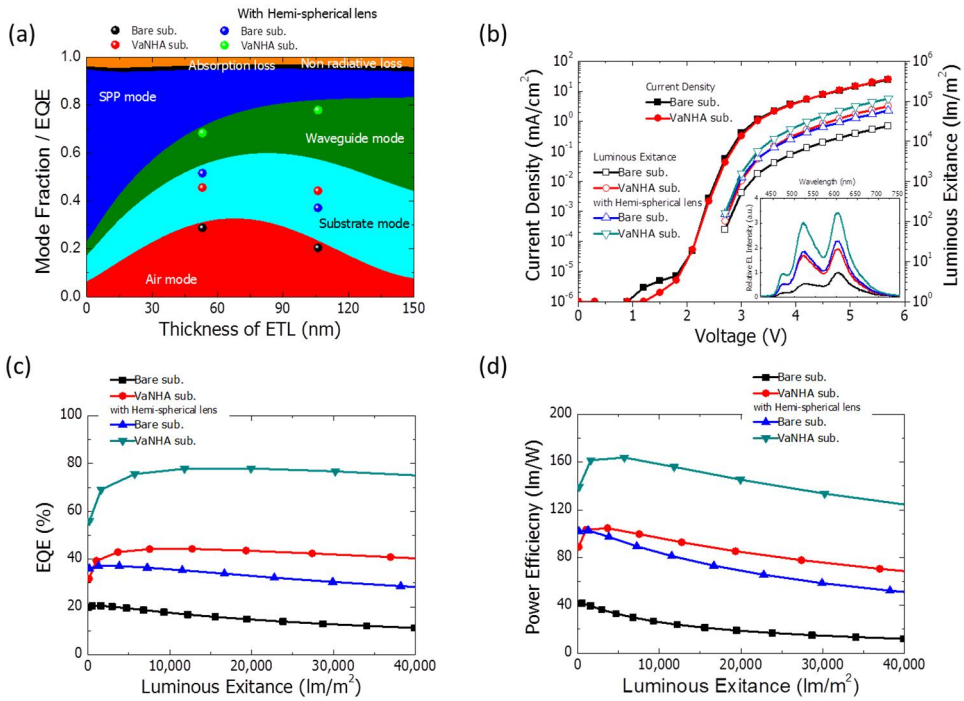

Figure 4.4 (a) Simulated mode fraction as a function of the thickness of ETL (lines) without light extraction layers and maximum external quantum efficiencies of WOLED I and II. (b) Current density-voltage-luminous exitance characteristics of the WOLEDs II w/ and w/o VaNHA and half-spherical lens. Inset: Relative EL spectra of device w/o and w/ VaNHA and lens at 3 mA/cm^2 in an integrating sphere. (c) EQEs of the WOLEDs with/without VaNHA and half-spherical lens as a function of luminous exitance. (d) Luminous efficacies of WOLEDs w/o and w/ VaNHA and half-spherical lens as a function of luminous exitance.

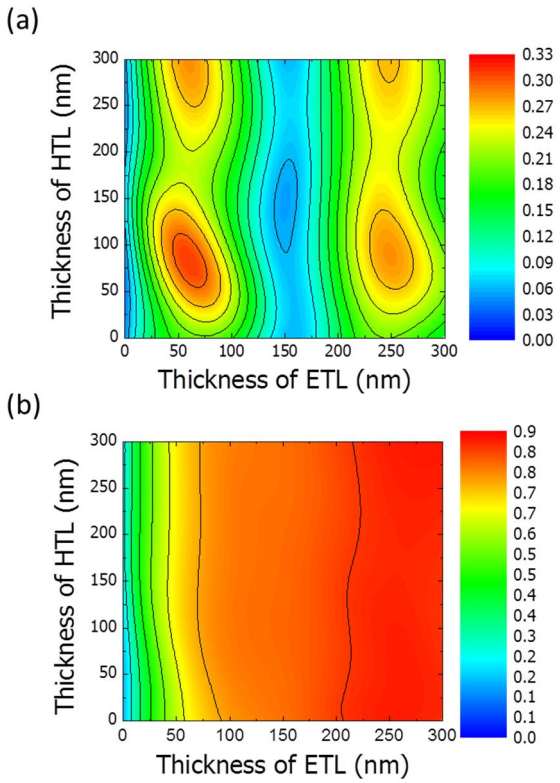

Figure 4.5 Contour plots of extraction efficiency as functions of ETL (B3PYMPM) and HTL (TAPC) thicknesses. (a) Air mode and (b) extractable mode (sum of air, substrate and waveguide mode). The recombination zone was assumed to be located in the middle of the orange and blue emission layers. Device structure was the same as Figure 4.2 with varying thicknesses of TAPC and doped B3PYMPM layers. The exciton density ratios of the blue, green, and red emitters were assumed to be 0.14, 0.26 and 0.60.

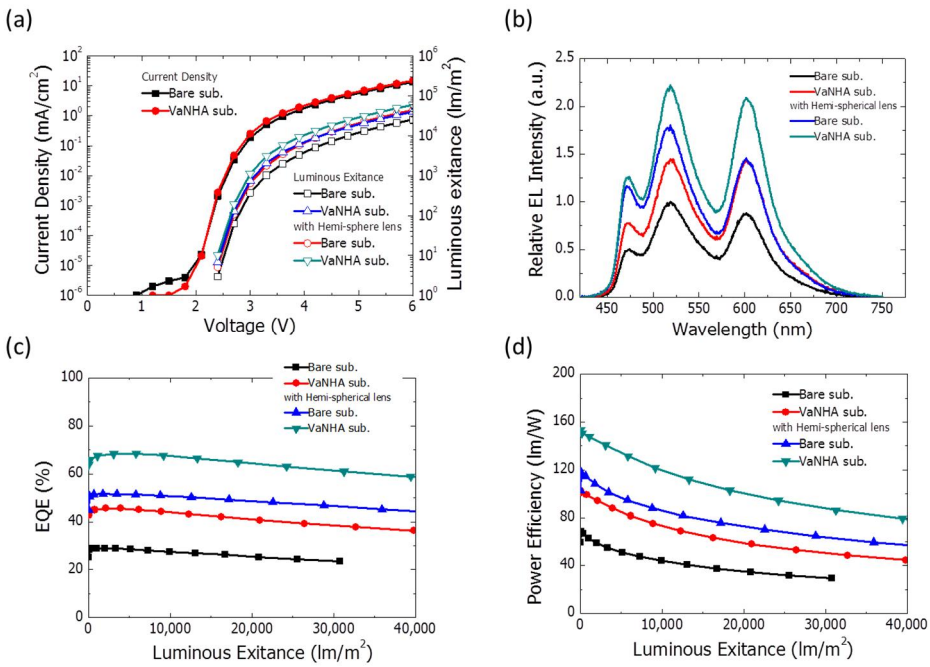

Figure 4.6 (a) Current density-voltage-luminous exitance characteristics of the WOLEDs I w/ and w/o VaNHA and lens. (b) Relative EL intensities of the device w/o and w/ VaNHA and lens at 3 mA/cm^2 measured in an integrating sphere. (c) EQEs of the WOLEDs with/without VaNHA and lens as a function of luminous exitance. (d) Luminous efficacies of WOLEDs w/o and w/ VaNHA and lens as a function of luminous exitance.

emission to a specific direction, thus luminous exitance (lm m^{-2}) was measured instead of luminance (cd m^{-2}). The *J–V* curves of the WOLEDs with and without the VaNHA are the same because of the smooth Si_3N_4 surface with little roughness, clearly indicating that the embedded VaNHA has no descrimental effect on device lifetime. Inset of Figure 4.4 (b) shows the relative EL intensities of WOLED II measured in an integrating sphere at 3 mA cm^{-2} and Figure 4.4 (c) and (d) represent the EQEs and the LEs of the WOLED with and without the VaNHA and a hemi-spherical lens on the glass substrate as a function of luminous exitance. The overall efficiencies of WOLED II are summarized in Table 4.1.The WOLED II with and without the VaNHA showed the maximum EQEs of 20.5 and 44.3%, respectively. The EQE of the WOLED II w/o the VaNHA is lower than WOLED I w/o VaNHA because the device is not optimized for the maximum air mode but optimized for large extractable mode. In combination with half spherical lens to reduce the total internal reflection at the glass/air interface, the WOLED II w/o and w/ the VaNHA showed maximum EQEs of 37.1 and 78.0% respectively. The enhancement ratios were 2.16 (w/ VaNHA), 1.8 (w/ half spherical lens) and 3.80 (w/ VaNHA and half spherical lens), respectively. The LEs of the WOLED II w/o and w/ VaNHA at 1,000 cd m^{-2} are 32.4 and 101 lm W^{-1} respectively. In combination with the half spherical lens, the WOLEDs w/o and w/ the VaNHA showed the LEs of 94.3 and 163 lm W^{-1}. The enhancement ratios were 3.11 (w/ VaNHA), 2.77 (w/ half spherical lens) and 5.03 (w/ VaNHA and half spherical lens), respectively.

Table 4.1. Performance of WOLEDs II w/o and w/ VaNHA and half spherical lens at luminance of 1,000 cd m^{-2}, except maximum PE and EQE.

VaNHA	Half spherical lens	Voltage [V]	J [mA/cm^2]	PE [lm W^{-1}]	CIE		EQE [%]
					x	y	
w/o	w/o	3.96	4.01	32.4	0.545	0.425	19.3
w/o	w/	3.42	1.60	94.3			36.9
w/	w/o	3.51	1.80	101.1	0.442	0.475	43.9
w/	w/	3.34	1.18	162.9			75.9

The maximum EQEs of the WOLEDs without and with the VaNHA and the half spherical lens are displayed as data points in Figure 4.4 (a). The EQEs of the WOLEDs w/o the light extraction structure matched well with the calculation results (air mode). Interestingly the extracted lights with the VaNHA are almost the same regardless of the ETL thickness probably because the internal extraction layer breaks the cavity mode of the WOLEDs. The devices with the half spherical lens and the VaNHA extracted all the glass and WG modes and achieved almost theoretical maximum extractable efficiency up to 78% with the ETL thickness of 105 nm (WOLED II). To the best of our knowledge, these are the highest reported efficiencies in literature (Figure 4.7 and Table 4.2) and are almost comparable with the LEs of LEDs.[84]

Color quality of WOLED with VaNHA

Figure 4.8 shows the normalized electroluminescent spectra of the WOLEDs w/o and w/ the VaNHA at 1,000 cd m^{-2}, respectively. The emission spectra of the WOLEDs with a bare substrate show large variation with increasing thickness of the ETL due to the weak microcavity effect. The correlated color temperature (CCT) was significantly reduced from 2670 K (WOLED I) to 1930 K (WOLED II) as the thickness of the ETL increases. However, the WOLEDs with VaNHA show significantly reduced spectral change and a high CCT of 3400 K was realized from WOLED II. The CRI values of the devices w/ and w/o VaNHA are high with 78 and 81, respectively. This feature that the color quality of an OLED with VaNHA is

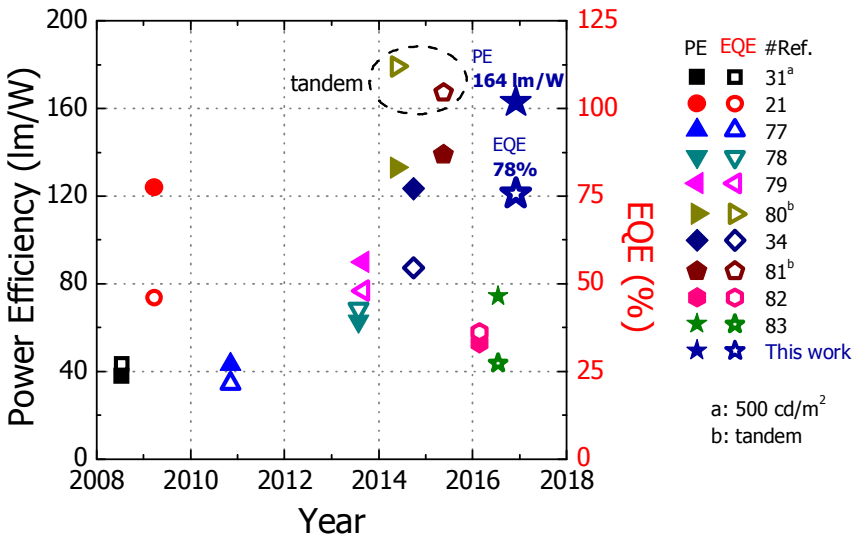

Figure 4.7 Comparison of the efficiencies of WOLEDs demonstrated in this work with the state-of-the-art WOLEDs.[31,21,77-80,34,81-83]

Table 4.2 Performances of WOLEDs with light extraction structure reported in literature.

Light extraction structures	CRI	PE[a] [lm W^{-1}]		EQE[a] [%]		Ref.
		w/o external extraction	w/ external extraction	w/o external extraction	w/ external extraction	
High refractive index substrate and lens	69	30	124	13.1	46	[21]
Graphene electrode, high refractive index substrate and lens	85	-	90	17	48	[79]
High-n light outcoupling texture and optimized microstructure	84	-	133	-	112[b]	[80]
Internal and external deterministic aperiodic nanostructures	-	90	123.4	38	54.3	[33]
Internal scattering layer and external extraction layer	81	-	139	-	-	[81]
Vacuum nano-hole array and lens	78	101.1	162.9	43.9	75.9	This work

a) measured at 1,000 cd m^{-2}
b) tandem device

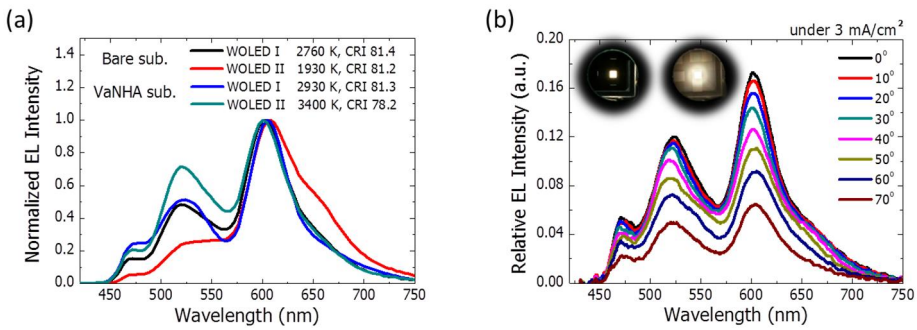

Figure 4.8 (a) Normalized electroluminescence (EL) spectra of WOLED I and II without and with VaNHA measured in the normal direction to the glass substrates at 1,000 cd m^{-2}. The CCT and CRI are given for each spectrum. (b) Angle dependent EL spectra of WOLED II with VaNHA. Inset: Photographs of the WOLEDs with (left) and without VaNHA (right).

not sensitive to the thickness of the device can provide a wide process window for practical application. The emission images of the WOLEDs are shown in the inset of Figure 4.8 (b) for the devices without and with the random VaNHA. The WOLEDs with random VaNHA showed the uniform but diffused emission pattern as predicted by the 2D-FFT in Figure 4.1 (b). The emission spectra of WOLED II with the randomly distributed VaNHA showed very little spectral change with viewing angle (Figure 4.8 (b)). All the luminous characteristics (CCT of 3400 K, CRI ~80, uniform emission pattern, little variation of color with viewing angle) demonstrate that the WOLEDs satisfy the requirements as a high quality light source.

4.4 Optical simulation for extraction efficiency of waveguide mode

To analyze the extraction mechanism of the OLEDs with VaNHA, we carried out the FDTD calculation by varying the refractive index of the dielectric material of the extraction layer from 1.3 to 2.3, and observed the behavior of the waveguide mode. The FDTD calculation details are described in methods. Figure 4.9 shows the distribution of the electric field inside the OLEDs after 100 fs from the start of the dipole emission. VaNHA is inserted between the substrate and the ITO electrode and mainly influence the waveguide mode, thus the analysis is a good tool to understand the extraction mechanism. 100 fs is an enough time for the air and substrate modes to escape to the outside. Therefore the distribution of the electric field displays the developed waveguide mode inside of the device after the time. In a device with bare glass wafer, the waveguide mode still exists when the dielectric layer have the refractive index smaller than 1.7 even if VaNHA is embedded. This is because the distance between the trapped light and the scattering medium is so large that the evanescent field cannot penetrate to the VaNHA. As the refractive index of the dielectric layer increases, the vertical distribution of the waveguide mode becomes longer (deep penetration of the evanescent field) as shown in Figure 4(b)-4(g), and finally, when the refractive index of the waveguide mode is higher than 1.9, the confined wave is not observed in the transparent conducting oxide (TCO) layer anymore. The waveguide mode confined near the TCO is extracted through a high-index material, and then interacts with VaNHA

during multiple reflections to have an opportunity to extract to the air. However, too high refractive index of the dielectric layer will reduce the coupling probability of the scattered light to the substrate to increase the cycling of the scattered light in the dielectric, TCO and organic layers before escaping to air, resulting in increased absorption. Therefore, the optimum refractive index of the dielectric layer to extract light efficiently is the one close to that of TCO layer. The FDTD analysis confirms that the selected Si_3N_4 having a refractive index of 2.02 is an optimum material as VaNHA substrate maximizing the extraction efficiency.

To analyse extraction tendency, enhancement ratios with various refractive index of dielectric layer and nanohole array are calculated using FDTD. Contour plot of enhancement is in Figure 4.10. The improvement of the light extraction efficiency was found to be increased as the refractive index of the nano-hole array was lower and the refractive index of the dielectric layer was higher. When the refractive index of the dielectric layer was 1.9 or more, the light extraction efficiency was the highest. Calculated enhancement ratio is similar to enhancement ratio calculated by the classical electric dipole model and the enhancement ratio obtained by the experiment. Interestingly, the larger the refractive index difference is, the larger the improvement in the light extraction efficiency is obtained even in the region where the refractive index of the nano hole array is higher than the refractive index of the dielectric layer. However, there are few materials that can realize a low refractive index substrate with a refractive index of 1.4 or less and a high refractive index nano hole array with a refractive index of 2.1 or higher. Figures 4.10 (b) and (c) show the results obtained by changing the refractive index

of the nanohole by fixing the refractive index at 1.0 and changing the refractive index of the dielectric layer, and by changing the refractive index of the dielectric layer to 2.0 and changing the refractive index of the nanohole.These simulation results prove that Si_3N_4 and vacuum is proper material for realizing large enhancement of extraction efficiency.

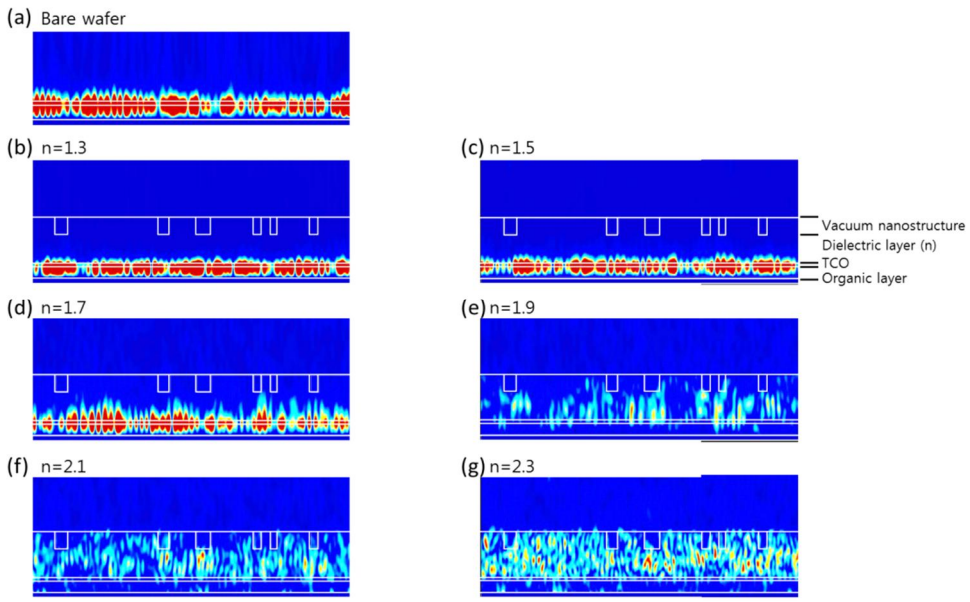

Figure 4.9 (a) Electric field of WOLEDs with bare glass substrate. (b-g) Electic field of WOLEDs with a VaNHA substrate having different refractive index of dielectric material, $n_{dielectic\ material}$=1.3, 1.7, 1.9, 2.1 and 2.3, respectively.

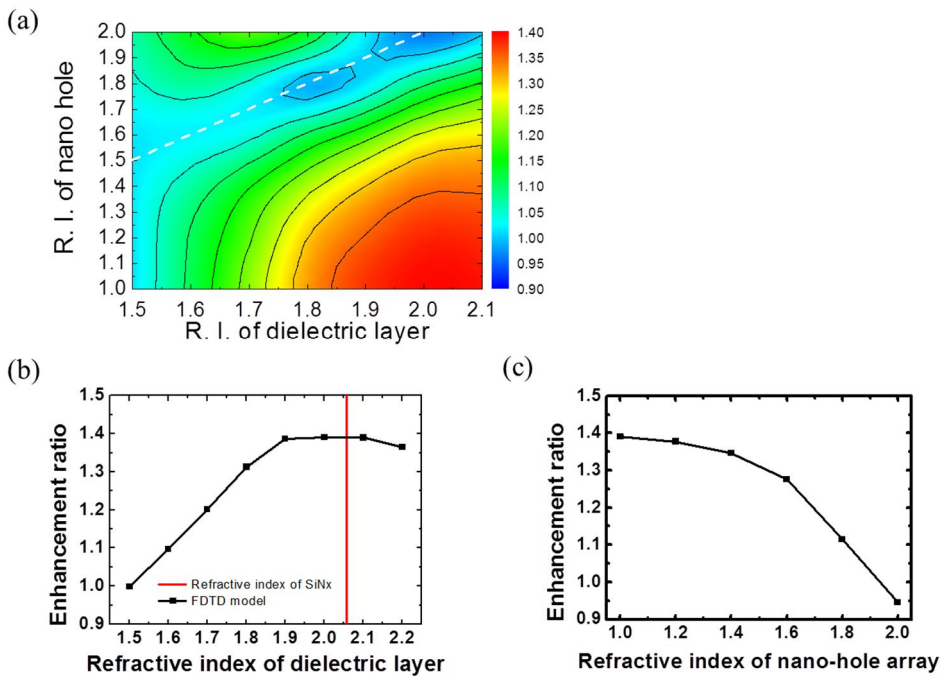

Figure 4.10 (a) Contour plot of enhancement ratio with various refractive index of dielectric layer and nanohole array. White dotted line is area where refractive index of dielectric and nanohole is same. Enhancement ratio (b) with refractive index of dielectric layer (refractive index of hole is fixed as 1.0.) and (c) with refractive index of hole array (refractive index of dielectric layer is fixed as 2.0).

4.5 Conclusion

In summary, high performance WOLEDs with the EQE of 76% and the LE of 163 lm W^{-1} at 1000 cd m^{-2} are realized using a random VaNHA in combination with a half spherical lens. To the best of our knowledge, these values (EQE_{max} of 78% and LE_{max} of 164 lm W^{-1}) are the highest reported efficiencies in literature and are comparable with the LEs of LEDs. The WOLEDs showed low efficiency roll-off, low operating voltage. The random pattern is designed to have no specific symmetry in the reciprocal space. Base on the design, we could realize a high quality light source with uniform emission, high CCT of 3400 K, high CRI of around 80, and no color varation with viewing angle. The radom VaNHA structure guarantees no additional electrical degradation compared to the device without VaNHA. FDTD analysis indicated that combination of vacuum hole and planarization layer with the refractive index similar to the refractive indices of organic material and ITO extracted waveguide mode effectively.

Chapter 5. Tandem white organic light emitting diode with high color quality and efficiency

5.1 Introduction

White organic light emitting diode (WOLED) is supposed as alternative lighting materials for being high power efficiency, free from mercury, glare, flickering and ultra violet (UV) emission and applicability to flexible substrate. From Kido et al.'s first report of white OLED,[84] efficiency of WOLED progressed constantly and reached efficiency comparable to LED efficiency.[79-81]

For achieving highly efficient WOLED, various device structures have been reported such as single EML device,[85,86] stacked EML devices,[83,87,88] blue emitting device with down conversion layer,[89] parallel device with single devices[90] and tandem device[91-94]. Single or multiple EML devices have strength in simplicity of device structure design but, color stability with operating voltage is poor due to increased ratio of direct trapping to each dopant. Blue OLED with yellow down conversion is strength in minimized materials needed and extraction efficiency with phosphor but has weakness at low efficiency and lifetime of blue emitting OLED. Parallel device has strength in color quality control by area ratio of each pixel and operating voltage but, needs fine pixel area for realizing white color to human eye. Tandem device which consists of multiple devices with charge

generation layer (CGL) has weakness at complicated davice structure and voltage loss at CGL, but has strength at long life time and color stability due to low current density at each unit. In addition, efficienct CGL has been reported recently.[95] Tandem WOLED is promised applicable structure for WOLED.

In order for white OLED to be applied to lighting, not only light extraction efficiency but also the color quality of white light is important. The color quality can be divided into two parts: chromacity and redition (Figure 5.1).[96] To improve the color quality, some strategies have been reported such as synthesizing new molecules,[93,97] increased the number of dye.[88,98] Figure 5.2 shows the distribution of CIE coordinates of the white OLED reported and the CRI, CCT and power efficiency. High CRIs were formed mainly in the range of low color temperature (~3,000 K). Warm white is applicable to indoor lighting but is limited in usage for various environments. Also, low color temperature and high CRI are not favored in terms of color preference.[96] In respect of chromacity, Macadam ellipse which is defined as the indistinguishable area by human eye is important factor for color quality. There were not many studies with color coordinates in the macadam ellipse. Therefore, research on color quality is still necessary. Cho et al. have reported the color quality of WOLED by calculating the CRI through the PL spectral sum of the dopants used.[93] In most cases, the color quality obtained from device are distorted from spectrum of PL sum due to the micro cavity structure.

In this study, we report an analytical modeling of the color quality of WOLED

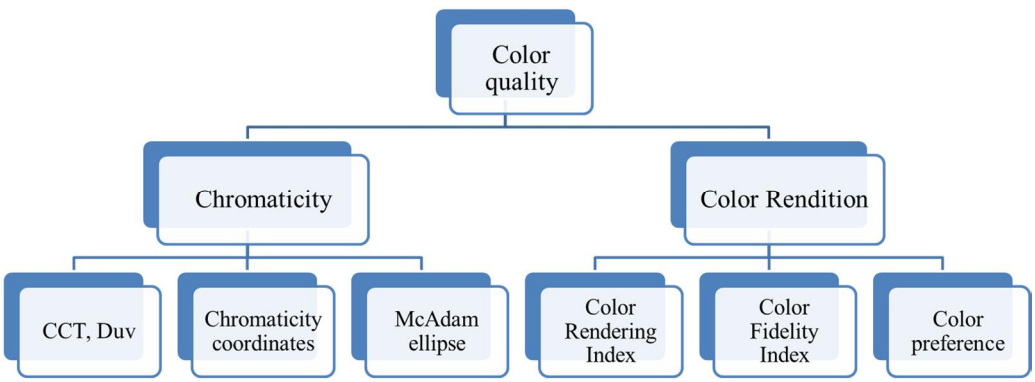

Figure 5.1 Parameters of color quality in lightings.

(a)

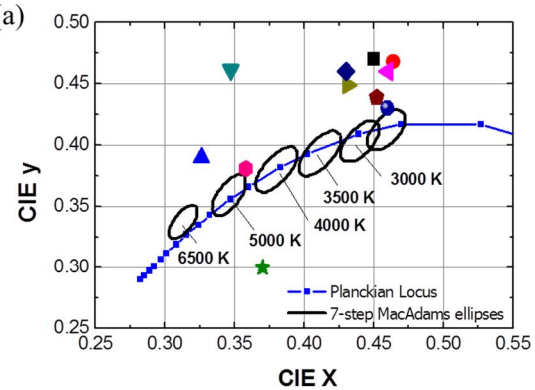

(b)

#	CRI	CCT [K]	PE [lm/W]	Ref.
1 ■	80	-	30	[21]
2 ●	86.5	3050	51	[79]
3 ▲	41	5685	41	[95]
4 ▼	51	5212	60	[34]
5 ◀	92	2968	22	[98]
6 ▶	92	-	63.2	[88]
7 ◆	85	-	74.5	[83]
8 ⬟	90.9	-	38.34	[93]
9 ●	95	-	13	[99]
10 ★	84.6	5883	5 [EQE]	[100]
11 ●	88.6	2780	19.5	[94]

Figure 5.2 (a) Reported CIE color coordinate of state-of-the-art WOLEDs and (b) corresponding CRIs, CCTs and PEs.

with presence or absence of light extraction structures. The spectra of device without and with light extracting structures are calculated by classical electromagnetic dipole modeling.[61-63] Each light extracting structure includes a hemispherical lens, a high refractive index substrate and index lens, a high refractive index substrate and lens with thick ETL which represent spectra when substrage mode, waveguide and SPP modes are additionally extracted. Based on the spectrum obtained from this calculation, the accuracy of the model was compared with the spectrum of the experimental result, and the tendency when the light extraction was applied was analysed. With optical analysis, we demonstrated white tandem OLEDs with high efficiency of 38 lm W-1 and high color quality of CRI 80 with CCT over 6,000 K.

5.2 Optical simulation for achievable color quality

The molecular structure and spectrum of the dye used in this calculation and the color coordinates of each spectrum are shown in Figure 5.3. $Ir(mphmq)_2(tmd)$ and $Ir(3',5',4\text{-}mppy)_2(tmd)$, FIrpic and FCNIrpic represent Iridium(III)bis(4-methyl-2-(3,5-dimethylphenyl) quinolinato-N,C2') tetramethylheptadionate, bis(2-(3,5-dimethylphenyl)-4-methylpyridine) Ir(III)(2,2,6,6-tetramethylheptane-3,5-diketonate), (Iridium(III) bis((4,6-di-fluorophenyl)-pyridinato-N,C')) and Iridium(III) Bis[(5-cyano-4-fluorophenyl)pyridinato-N,$C^{2'}$]picolinate, respectively.[101,102] $Ir(mphmq)_2(tmd)$, $Ir(3',5',4\text{-}mppy)_2(tmd)$ and FCNIrpic are used as red, green and FIrpic is used for comparison with FCNIrpic. The PL quantum yield of $Ir(mphmq)_2(tmd)$, $Ir(3',5',4\text{-}mppy)_2$tmd, FCNIrpic and FIrpic are 96, 97, 96 and 97%, respectively. The horizontal emitting dipole ratios of $Ir(mphmq)_2(tmd)$, $Ir(3',5',4\text{-}mppy)_2$tmd, FCNIr and FIrpic are 82, 80, 76 and 76%, respectively. WOLED with FCNIrpic is expected to have higher CRI based on a blue shifted spectrum of FCNIrpic compared to device with FIrpic (Figure 5.3 (b)). When Firpic is used, the main peak and shoulder peak are close to 500 nm and the CIE y coordinate is 0.35, and the spectral distribution obtained using this does not cover the Planckina locus. On the other hand, FCNIrpic is expected to be able to realize better white color by including the full range of Planckina locus (Figure 5.3 (c)).

First, we analyzed the trend of CRI according to the ratio of photons of the red, green and blue dopants in the WOLED. Since the devices used in this study are combined with internal and external light extraction methods, microcavity effect

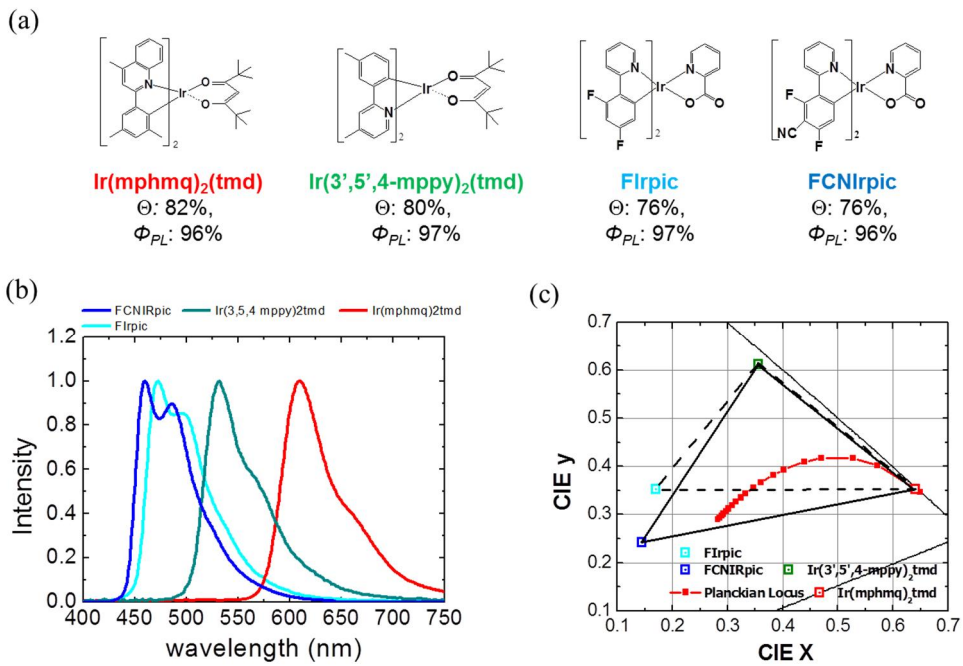

Figure 5.3 (a) Molecular structure, PLQY, horizontally oriented dipole ratio of phosphorescent dyes (b) corresponding spectrum and (c) CIE cordintaes.

which is depending on the thickness of organic layers is minimized. Surface plasmon polariton (SPP) loss is also minimized by elongating the distance between emitting dipoles and reflective electrode. The extracted light from white device is assumed to be similar with PL spectral sum according to photon ratio of red, green and blue dopants.

$$\text{Spectrum} = \text{PL}_\text{B} \times x + \text{PL}_\text{G} \times y + \text{PL}_\text{R} \times (1 - x - y) \quad (3)$$

PL_G, PL_R and PL_B mean the spectrum of green, red and blue dopants, respectively. And x and y means the relative ratio of blue and green photons. After extracting the CIE x, y, and CRI of the spectrum, we plotted a contour plot for CRI over the CIE coordinates in Figure 5.4. The maximum CRI of WOLED obtained using FCNIrpic and FIrpic is 95 and 90 whose corresponding CIE coordinates are (047, 0.45) and (0.45, 0.42). In WOLED with FIrpic, contour plot shows that the region where the CRI is highly formed is far away from the Macadam ellipse. On the other hand, the region of CRI 90 is contained within the macadam ellipse in WOLED with FCNIrpic.

In order to analyze the tendency of color quality change by micro cavity structure, we calculated the classical electromagnetic dipole model by applying the following extraction structures. The light extraction structures implemented in the calculations are shown in Figure 5.5. The spectra corresponding to the viewing angles of the device without the light extracting structure were calculated at intervals of 2° and the total spectrum was obtained considering the solid angle

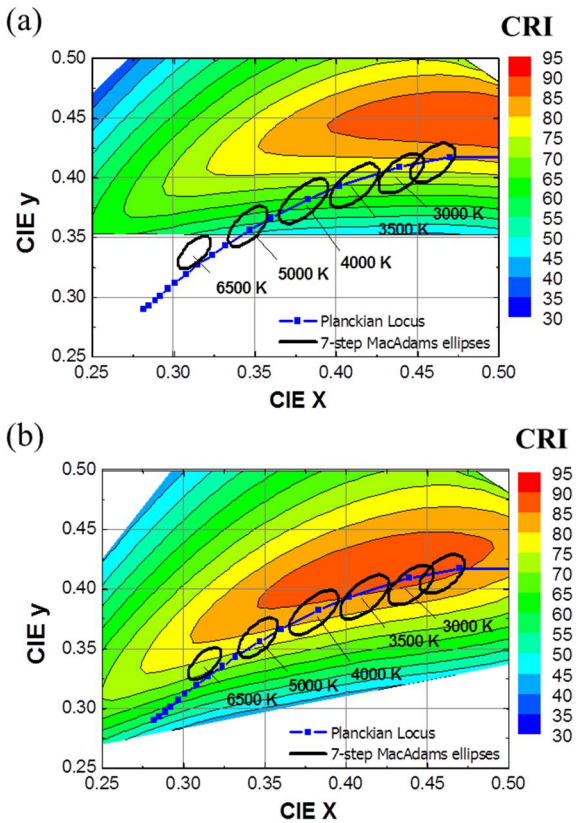

Figure 5.4 (a) Contour plot of acheivable CIE coordinate and CRI with combination of Ir(mphmq)$_2$tmd, Ir(3',5',4-mppy)$_2$tmd and FIrpic. (b) Contour plot of acheivable CIE coordinate and CRI with combination of Ir(mphmq)$_2$tmd, Ir(3',5',4-mppy)$_2$tmd and FCNIrpic.

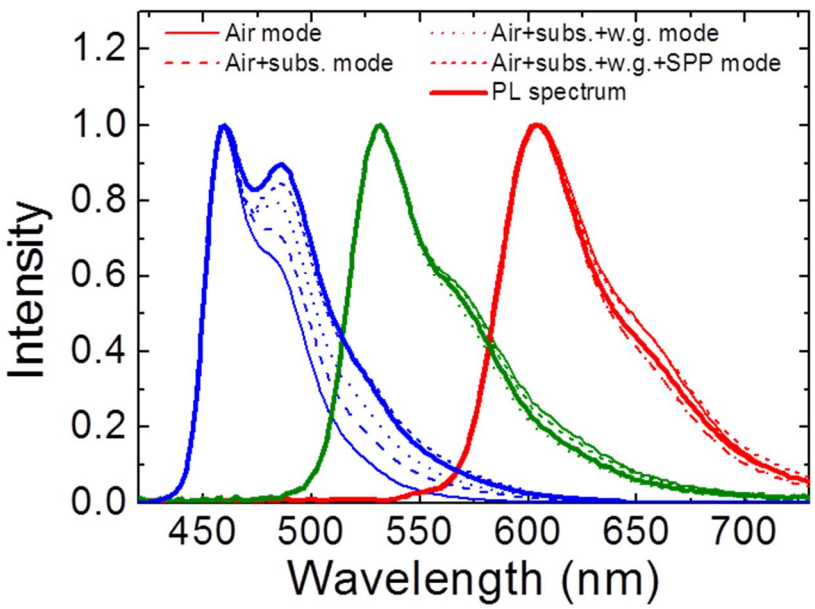

Figure 5.5 Calculated spectrum of R, G, B dyes in WOLED with various light extraction structure.

which is same with spectrum measured at integrating sphere. Next, the spectra applied with the hemispherical lens were obtained by setting the thickness of the glass to semi-infinite in the calculation. This is the same as the extracted spectrum for all the air and substrate modes. The refractive index of the glass substrate was changed to high refractive index (1.8 or more) and the spectrum was calculated using the same medium as the high refractive index substrate. This is the same spectrum as the combined high refractive index substrate and high refractive index lens in the experiment and the spectrum when the air, substrate and waveguide mode are fully extracted. The SPP mode is not easy to extract entirely due to the high absorption of aluminum. Therefore, a device with a thick ETL is implemented to minimize SPP loss. Calculated spectrum is light in which air, substrate and wavueguide mode are extracted and SPP loss is minimized.

The results of dopant-specific spectral calculations obtained in each optical structure were compared to the PL spectra and included in Figure 5.6. In the case of green and red, there was a slight change in the pick according to the mode in the right shoulder pick. In the case of blue, the change of the shoulder pick dramatically. It can be seen from the calculation that the shoulder pick of the blue gradually increases in the direction in which the extracted light increases. SPP suppression did not reach the same as the PL spectrum, as some still remained.

Based on the spectrum obtained for each structure, the spectra were again calculated for each dopant ratio, and this was implemented as a CRI contour plot in the CIE space (Figure 5.7). When the air mode is extracted, unlike the dopant PL, it

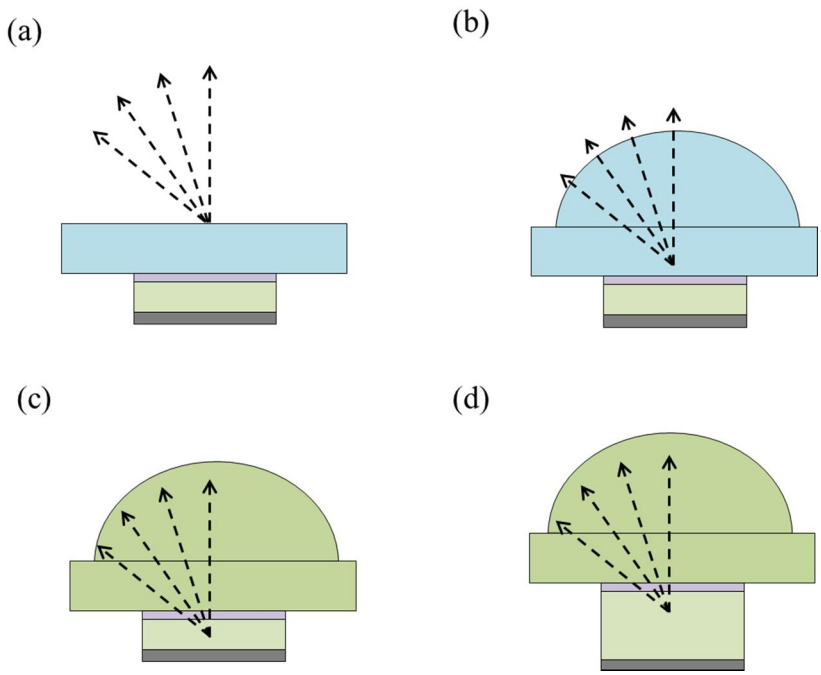

Figure 5.6 Schematic descriptions of (a) OLED without light extraction structure, (b) OLED with half-spherical lens, (c) OLED with high refractive index substrate and lens and (d) OLED with high refractive index substrate and lens with elongated electron transport layer.

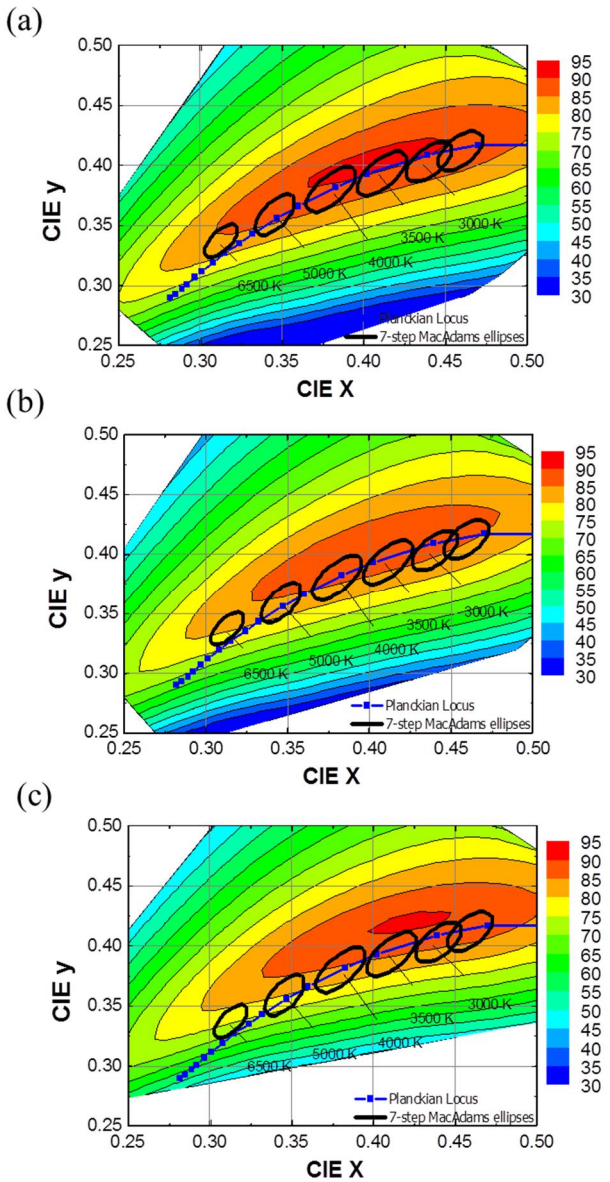

Figure 5.7 Contour plot of CIE coordinate and coresponding CRI of (a) WOLED without light extraction layer, (b) WOLED with half-spherical lens and (c) WOLED with high refractive index substrate and lens with elongated ETL.

is possible to see a broader color distribution due to the limited blue pick and an increase in the overall CRI value. As the light extraction structure is gradually applied, the cie spatial distribution gradually becomes narrower, and the CRI value according to the coordinates also approaches the combination of the dopant PL. This is a predictable part of the results of the spectral calculations.

5.3 Experiment

The OLEDs were fabricated on clean glass substrates pre-patterned with 70-nm-thick ITO under a pressure of 5×10^{-7} Torr using thermal evaporation without breaking the vacuum. The device and substrate area is 2×2 and 25×25 mm^2, respectively. OLED stacks are composed of 6 wt% ReO_3 doped mCP (20 nm) / mCP (20 nm)/ mCP:BM-A10:12 wt% FCNIrpic (30 nm) / BM-A10 (20 nm) / 9 wt% Rb2CO3 doped BM-A10 (25 nm) / 22.8 mol% Rb_2CO_3 doped Bphen (10 nm) / HATCN (20 nm) / TAPC (20 nm) / TCTA (10 nm) / TCTA:B3PYMPM:8 wt% Ir(3',5',4-mppy)$_2$tmd: 0.7 wt% Ir(mphmq)$_2$tmd (15 nm) / B3PYMPM (10 nm) / 1 wt% Rb_2CO_3 doped B3PYMPM (40 nm) / Aluminium (100 nm), where mCP, BM-A10, BPhen, HATCN, TAPC, TCTA and B3PYMPM are abbreviated forms of N,N'-dicarbazolyl-3,5-benzene, 2,4-bis(4-(diphenyl-phosphoryl)phenyl)pyridine, 4,7-Diphenyl-1,10-phenanthroline, 1,4,5,8,9,11-hexaazatriphenylene hexacarbonitrile, 1,1-bis-(4-bis(4-methyl-phenyl)-amino-phenyl)-cyclohexane, 4,4',4"-tris(carbazol-9-yl)triphenylamine and bis-4,6-(3,5-di-3-pyridyphenyl)-2-methylpyrimidine respectively (Figure 5.8).[103]

Current density-voltage-luminance characteristics and EL spectra were measured using a Keithley 2400 programmable source meter and a SpectraScan PR650 (Photo Research). The EQEs of the WOLEDs w/o half-spherical lens were measured using Keithley 2400 programmable source meter, rotation stage and Ocean Optics S2000 fiber optic spectrometer. The Enhancement ratios of EQE and LE of WOLEDs with Lens were measured with an integrating sphere and a

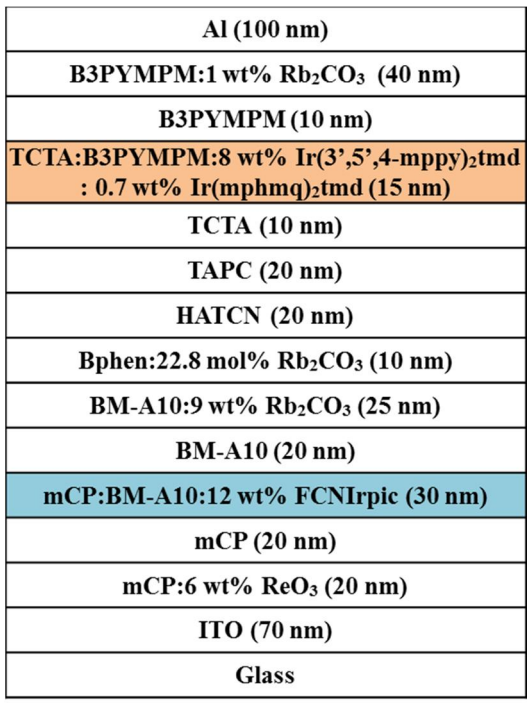

Figure 5.8 Devices structure of tandem white OLED.

monochromator attached photomultiplier tube (PMT) as an optical detector system. A hemisphere lens with a diameter of 10 mm is attached on the glass surface with index matching oil.

5.4 Result and Discussion

Figure 5.9 (a) shows electroluminescent (EL) spectra of OLEDs without and with at integrating sphere. The calculated spectra were well fitted except for the relative ratio of the blue spectrum obtained from the experimental results. This difference is presumably because the blue emission zone set in the calculation is different from the experiment. The corresponding CIE coordinates, CCTs and CRIs of the devices were (0.281, 0.307) and 9,057 K, and (0.303, 0.351) and 6,840 K for device without and with lens, respectively (Figure 5.9 (b)). These colours are daylight white. The WOLEDs exhibited high CRI values of 80 and 82 for device without and with lens, respectively, which are sufficient for high quality light sources. Even though the devices are not within the 7-step MacAdams ellipses, they are close enough for solid state lighting. The color quaility obtained by experiments and calculations is shown in Table 5.2. Although the color quality is not obtained by applying the internal light extraction structure as an experiment, it can be expected that the CCT increases and the CRI decreases as more light is extracted through calculation. This tendency is consistent with the tendency to increase the second peak of FCNIrpic as the light extraction efficiency is enhanced.

The current density-voltage-luminance (J-V-L) characteristics of the WOLEDs are shown in Figure 5.10. The operating voltages were low at 5.1 and 6.67 V at turn-on and 1,000 cd/m^2 for WOLED without lens, respectively. Figure 5.10 (b) shows the EQEs and the PEs of the WOLEDs. The WOLEDs showed maximum EQEs of 45.6 and 79.4% and maximum LE of 48.9 and 94.0 lm/W for

WOLED without and with lens, respectively. These values are higher than that of fluorescent tubes. Moreover, it is better for the human eye because it does not contain the UV region (380-420 nm) light. The performances of the devices are summarized in Table 1. The EQEs achieved here represent the highest yet reported in the literature with high CCT over 5,000 K and high CRI over 80.

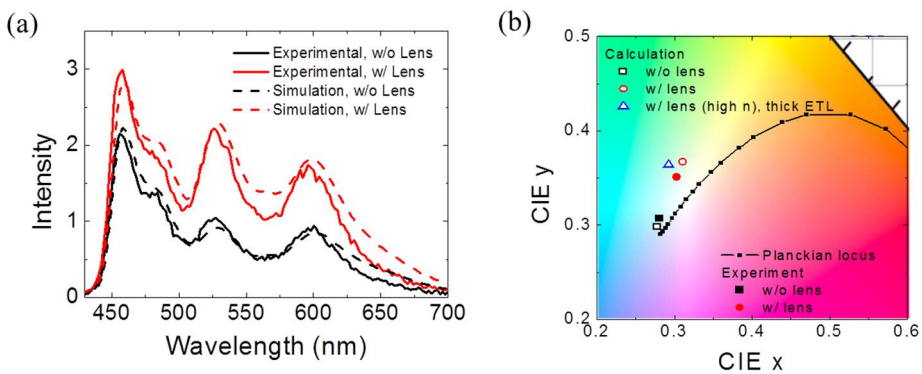

Figure 5.9 (a) EL spectrum of WOLED without and with Lens and calculated spectrum of corresponding devices (b) Color coordinates of WOLEDs without and with light extraction structure from experiment and calculation.

Table 5.1 Color coordinate, CCT and CRI of WOLEDs without and with light extraction structure from experiment and simulation.

	Structure	CIE x	CIE y	CCT	CRI
Experiment	w/o lens	0.281	0.307	9057	82.3
Experiment	w lens	0.303	0.351	6840	83.1
Simulation	w/o lens	0.278	0.298	9800	75.9
Simulation	w lens	0.311	0.367	6360	81.7
Simulation	w lens (high n)	0.286	0.360	7550	76.3
Simulation	w lens (high n) and thick ETL	0.292	0.364	7210	77.9

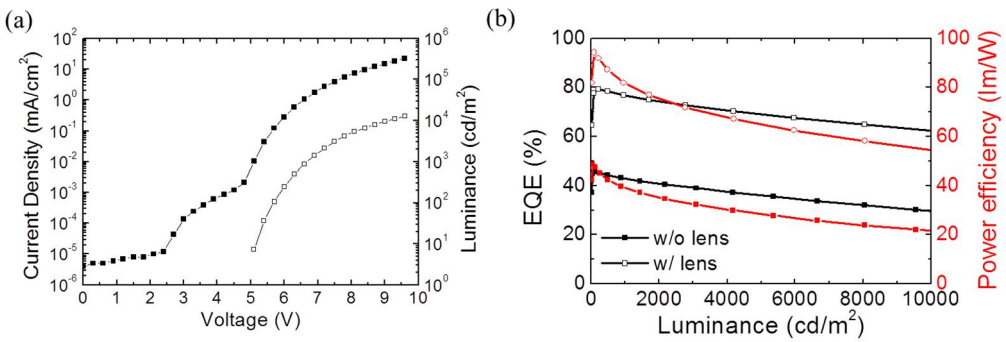

Figure 5.10 (a) J-V-L of WOLEDs without and with half spherical lens and (b) EQEs and Power efiiciencies with function of luminance of WOLEDs without and with lens.

Table 5.2 Performance of tandem WOLEDs without and with half-spherical lens (HS) of 1,000 cd/m^2.

Devices	Voltage [V]	J [mA cm^{-2}]	PE [lm W^{-1}]	CIE		EQE [%]
				x	y	
WOLED	6.67	1.27	38.9	0.281	0.307	42
WOLED (HS)	6.38	0.67	81	0.303	0.351	76

5.5 Conclusion

We report the theoretically achievable color quality of white tandem devices with various light extraction structure. First, color quality according to the proportion of the emitting dyes was calculated which is ideal value whole photolumeniscent (PL) spectrum is extracted. In consideration of micro cavity, achievable color quality of device without light extraction layer, device with half spherical lens, device with high refractive index and lens, device with high refractive index substrate and lens and elongated distance with dipole and metal electrode. The stronger the micro cavity structure, the lower the shoulder peak of FCNIrpic. Simulation result is compared with experiment result and matched well. By based this model, high efficiency tandem OLED with high color temperature (> 5,000 K) and high CRI (> 80) can be fabricated.

Appendix

Simulation codes of WOLED with VaNHA in FDTD Solutions.

```
deleteall;

calculation_width_x=10*10^-6;
calculation_width_y=10*10^-6;

addfdtd; #simulation structure
set("x", 0);
set("y", 0);
set("x span", calculation_width_x);
set("y span", calculation_width_y);
set("z min", %calculation_zmin%);
set("z max", 0*10^-6);
set("x min bc", "metal");
set("x max bc", "metal");
set("y min bc", "metal");
set("y max bc", "metal");
set("z min bc", "pml");
set("z min bc", "pml");
set("pml type","stretched coordinate PML");
set("pml profile",4);
set("pml kappa", 10);
set("pml sigma", 0.1);
set("pml layers", 32);
set("pml min layers", 32);
set("extend structure through pml", 0);
set("auto shutoff min", 0.0001);
set("same settings on all boundaries", 0);
set("pml min layers",32);
set("simulation time", %calculation_time%);
set("mesh accuracy", %mesh_accu%);

addpower; #Transmittance monitor
set("name", "T");
set("monitor type","2D Z-normal");
set("x", 0);
set("y", 0);
set("x span", calculation_width_x + 2*10^-6);
set("y span", calculation_width_y + 2*10^-6);
```

```
set("z", -500*10^-9);
set("output Ex", 1);
set("output Ey", 1);
set("output Ez", 1);
set("output Hx", 1);
set("output Hy", 1);
set("output Hz", 1);
set("output Px", 1);
set("output Py", 1);
set("output Pz", 1);
set("output power", 1);
set("override global monitor settings",1);
set("frequency points", 21);

addrect; #substrate
set("name","Substrate");
set("index",%substrate_index%); #refractive index of substrate
set("x", 0);
set("y", 0);
set("x span", calculation_width_x + 7*10^-6);
set("y span", calculation_width_y + 7*10^-6);
set("z min", -%substrate_h%);
set("z max",3*10^-6);

current_h= -%substrate_h%;

if(%include_VaNHa%==1) { #include or not include extraction layer
addrect; #SiNx
set("name","SiNx");
set("index",%SiNx_index%); #refractive index of dielectric layer
set("x", 0);
set("y", 0);
set("x span", calculation_width_x + 7*10^-6);
set("y span", calculation_width_y + 7*10^-6);
set("z max",current_h);
current_h=current_h - %SiN_h%;
set("z min", current_h);

current_h=current_h + %SiN_h% - %pc height%;

for (i=1:85) {
addcircle;
set("radius", 0.120*%scale micro%);
```

```
set("z min",current_h);
set("z max",current_h+%pc height%);
set("x", rand(-5,5)*%scale micro%);
set("y", rand(-5,5)*%scale micro%);
set("material", %void%);
set("name","post" + "");
set("override mesh order from material database",1);
set("mesh order",1);
addcircle;
set("radius", 0.150*%scale micro%);
set("z min",current_h);
set("z max",current_h+%pc height%);
set("x", rand(-5,5)*%scale micro%);
set("y", rand(-5,5)*%scale micro%);
set("material", %void%);
set("name","post" + "");
set("override mesh order from material database",1);
set("mesh order",1);
addcircle;
set("radius", 0.190*%scale micro%);
set("z min",current_h);
set("z max",current_h+%pc height%);
set("x", rand(-5,5)*%scale micro%);
set("y", rand(-5,5)*%scale micro%);
set("material", %void%);
set("name","post" + "");
set("override mesh order from material database",1);
set("mesh order",1);

current_h=current_h + %pc height% -%SiN_h%; }

addrect;
set("name","ITO");
set("material",%anode_material%);
set("x span",calculation_width_x + 7*10^-6);
set("y span",calculation_width_x + 7*10^-6);
set("z max",current_h);
current_h = current_h - %anode_h%;
set("z min",current_h);

addrect;
set("name","Organic");
set("material","<Object defined dielectric>");
```

```
set("index",1.8);
set("x span",calculation_width_x + 7*10^-6);
set("y span",calculation_width_x + 7*10^-6);
set("z max",current_h);
current_h = current_h - %organic_h%;
set("z min",current_h);

#red_hori
for(i=1:126) {
adddipole;
set("phi",0);
set("theta",90);
set("phase",20*round(rand(-0.5,8.5)));
set("set time domain",1);
set("pulse type", "standard");
set("frequency", 499.702*10^12);
set("pulselength", 10*10^-15);
set("offset", 40*10^-15 + rand(0,50)*10^-15);
set("x", rand(-(calculation_width_x-0.2*10^-6)/2,(calculation_width_x-
0.2*10^-6)/2));
set("y", rand(-(calculation_width_y-0.2*10^-6)/2,(calculation_width_y-
0.2*10^-6)/2));
set("record local field", 0);
set("z",current_h+%d_z%);
adddipole;
set("phi",90);
set("theta",90);
set("phase",20*round(rand(-0.5,8.5)));
set("set time domain",1);
set("pulse type", "standard");
set("frequency", 499.702*10^12);
set("pulselength", 10*10^-15);
set("offset", 40*10^-15 + rand(0,50)*10^-15);
set("x", rand(-(calculation_width_x-0.2*10^-6)/2,(calculation_width_x-
0.2*10^-6)/2));
set("y", rand(-(calculation_width_y-0.2*10^-6)/2,(calculation_width_y-
0.2*10^-6)/2));
set("record local field", 0);
set("z",current_h+%d_z%); }

#red_verti
for(i=1:55) {
adddipole;
```

```
set("phi",0);
set("theta",0);
set("phase",20*round(rand(-0.5,8.5)));
set("set time domain",1);
set("pulse type", "standard");
set("frequency", 499.702*10^12);
set("pulselength", 10*10^-15);
set("offset", 40*10^-15 + rand(0,50)*10^-15);
set("x", rand(-(calculation_width_x-0.2*10^-6)/2,(calculation_width_x-
0.2*10^-6)/2));
set("y", rand(-(calculation_width_y-0.2*10^-6)/2,(calculation_width_y-
0.2*10^-6)/2));
set("record local field", 0);
set("z",current_h+%d_z%); }

#green_hori
for(i=1:52) {
adddipole;
set("phi",0);
set("theta",90);
set("phase",20*round(rand(-0.5,8.5)));
set("set time domain",1);
set("pulse type", "standard");
set("frequency", 579.123*10^12);
set("pulselength", 10*10^-15);
set("offset", 40*10^-15 + rand(0,50)*10^-15);
set("x", rand(-(calculation_width_x-0.2*10^-6)/2,(calculation_width_x-
0.2*10^-6)/2));
set("y", rand(-(calculation_width_y-0.2*10^-6)/2,(calculation_width_y-
0.2*10^-6)/2));
set("record local field", 0);
set("z",current_h+%d_z%);
adddipole;
set("phi",90);
set("theta",90);
set("phase",20*round(rand(-0.5,8.5)));
set("set time domain",1);
set("pulse type", "standard");
set("frequency", 579.123*10^12);
set("pulselength", 10*10^-15);
set("offset", 40*10^-15 + rand(0,50)*10^-15);
set("x", rand(-(calculation_width_x-0.2*10^-6)/2,(calculation_width_x-
0.2*10^-6)/2));
```

```
set("y", rand(-(calculation_width_y-0.2*10^-6)/2,(calculation_width_y-
0.2*10^-6)/2));
set("record local field", 0);
set("z",current_h+%d_z%); }

#green_verti
for(i=1:29) {
adddipole;
set("phi",0);
set("theta",0);
set("phase",20*round(rand(-0.5,8.5)));
set("set time domain",1);
set("pulse type", "standard");
set("frequency", 579.123*10^12);
set("pulselength", 10*10^-15);
set("offset", 40*10^-15 + rand(0,50)*10^-15);
set("x", rand(-(calculation_width_x-0.2*10^-6)/2,(calculation_width_x-
0.2*10^-6)/2));
set("y", rand(-(calculation_width_y-0.2*10^-6)/2,(calculation_width_y-
0.2*10^-6)/2));
set("record local field", 0);
set("z",current_h+%d_z%); }

#blue_hori
for(i=1:27) {
adddipole;
set("phi",0);
set("theta",90);
set("phase",20*round(rand(-0.5,8.5)));
set("set time domain",1);
set("pulse type", "standard");
set("frequency", 637.894*10^12);
set("pulselength", 15*10^-15);
set("offset", 55*10^-15 + rand(0,50)*10^-15);
set("x", rand(-(calculation_width_x-0.2*10^-6)/2,(calculation_width_x-
0.2*10^-6)/2));
set("y", rand(-(calculation_width_y-0.2*10^-6)/2,(calculation_width_y-
0.2*10^-6)/2));
set("record local field", 0);
set("z",current_h+%d_z%);
adddipole;
set("phi",90);
set("theta",90);
```

```
set("phase",20*round(rand(-0.5,8.5)));
set("set time domain",1);
set("pulse type", "standard");
set("frequency", 637.894*10^12);
set("pulselength", 15*10^-15);
set("offset", 55*10^-15 + rand(0,50)*10^-15);
set("x", rand(-(calculation_width_x-0.2*10^-6)/2,(calculation_width_x-
0.2*10^-6)/2));
set("y", rand(-(calculation_width_y-0.2*10^-6)/2,(calculation_width_y-
0.2*10^-6)/2));
set("record local field", 0);
set("z",current_h+%d_z%); }

#blue_verti
for(i=1:17) {
adddipole;
set("phi",0);
set("theta",0);
set("phase",20*round(rand(-0.5,8.5)));
set("set time domain",1);
set("pulse type", "standard");
set("frequency", 637.894*10^12);
set("pulselength", 15*10^-15);
set("offset", 55*10^-15 + rand(0,50)*10^-15);
set("x", rand(-(calculation_width_x-0.2*10^-6)/2,(calculation_width_x-
0.2*10^-6)/2));
set("y", rand(-(calculation_width_y-0.2*10^-6)/2,(calculation_width_y-
0.2*10^-6)/2));
set("record local field", 0);
set("z",current_h+%d_z%); }

addpower; #Transmittance monitor
set("name", "Abs");
set("monitor type","2D Z-normal");
set("x", 0);
set("y", 0);
set("x span", calculation_width_x + 2*10^-6);
set("y span", calculation_width_y + 2*10^-6);
set("z", current_h);
set("output Ex", 1);
set("output Ey", 1);
set("output Ez", 1);
set("output Hx", 1);
```

```
set("output Hy", 1);
set("output Hz", 1);
set("output Px", 1);
set("output Py", 1);
set("output Pz", 1);
set("output power", 1);
set("override global monitor settings",1);
set("frequency points", 21);

addrect;
set("name","Al");
set("material",%cathode_material%);
set("x", 0);
set("y", 0);
set("x span", calculation_width_x );
set("y span", calculation_width_y );
set("z max",current_h);
current_h = current_h - %cathode_h%;
set("z min",current_h);

addmesh;
set("name","mesh_OLED");
set("x", 0);
set("y", 0);
set("x span", calculation_width_x);
set("y span", calculation_width_y);
set("z max", (0.02-%substrate_h%*10^6-0.8)*10^-6);
set("dx", %mesh_x%);
set("dy", %mesh_y%);
set("dz", %mesh_OLED_z%);

addmesh;
set("name","mesh_external");
set("x", 0);
set("y", 0);
set("x span", calculation_width_x);
set("y span", calculation_width_y);
set("z min", (0.02-%substrate_h%*10^6-0.8)*10^-6);
set("z max", 1*10^-6);
set("dx", %mesh_x%);
set("dy", %mesh_y%);
set("dz", %mesh_external_z%);
```

```
select("FDTD");
set("z min", current_h);
current_h = current_h - 380*10^-9;

select("mesh_OLED");
set("z min", current_h);
```

Biblography

[1] S.-Y. Kim, W.-I. Jeong, C. Mayr, Y.-S. Park, K.-H. Kim, J.-H. Lee, C.-K. Moon, W. Brütting, J.-J. Kim, *Adv. Funct. Mater.* **2013**, 23, 3896.

[2] M. A. Baldo, D. F. O'Brien, Y. You, A. Shoustikov, S. Sibley, M. E. Thompson, S. R. Forrest, *Nature* **1998**, 395, 151.

[3] H. Uoyama, K. Goushi, K. Shizu, H. Nomura, C. Adachi, *Nature* **2012**, 492, 234.

[4] C. K. Chiang, C. R. Fincher, Jr., Y. W. Park, A. J. Heeger, H. Shirakawa, E. J. Louis, S. C. Gau, A. G. MacDiarmid, *Phys. Rev. Lett.* **1977**, 39, 1098.

[5] J.-H. Lee, J.-J. Kim, *Phys. Status Solidi A* **2012**, 209, 1399.

[6] I. D. Parker, *J. Appl. Phys.* **1993**, 75, 1656.

[7] P. A. Hobson, S. Wedge, J. A. E. Wasey, I. Sage, W. L. Barnes, *Adv. Mater.* **2002**, 14, 193.

[8] P. T. Worthing. W. L. Barnes, *Appl. Phys. Lett.* **2001**, 29, 3035.

[9] C. F. Madigan, M. H. Lu, J. C. Sturm, *Appl. Phys. Lett.* **2000**, 76, 1650.

[10] T. Tsutsui, M. Yashiro, H. Yokogawa, K. Kawano, M. Yokoyama, *Adv. Mater.* **2001**, 13, 1149.

[11] L. H. Smith, J. A. Wasey, W. L. Barnes, *Appl. Phys. Lett.* **2004**, 84, 2986.

[12] S. Möller, S. R. Forrest, *J. Appl. Phys.* **2002**, 91, 3324.

[13] Y. Sun, S. R. Forrest, *J. Appl. Phys.* **2006**, 100, 073106.

[14] J.-B. Kim, J.-H. Lee, C.-K. Moon, S.-Y. Kim, J.-J. Kim, *Adv. Mater.* **2013**, 25, 3571.

[15] B. W. D'Andrade, J. J. Brown, *Appl. Phys. Lett.* **2006**, 88, 192908.

[16] T. Yamasaki, K. Sumioka, T. Tsutsui, *Appl. Phys. Lett.* **2000**, 76, 1243.

[17] J. J. Shiang, T. J. Faircloth, Anil R. Duggal, *J. Appl. Phys.* **2004**, 95, 2889.

[18] Y. H. Kim, J. Lee, W. M. Kim, C. Fuchs, S. Hofmann, H.-W. Chang, M. C. Gather, L. Müller-Meskamp, K. Leo, *Adv. Funct. Mater.* **2014**, 24, 2553.

[19] C.-H. Shin, E. Y. Shin, M.-H. Kim, J.-H. Lee, Y. Choi, *Opt. Express* **2015**, 23, A133.

[20] E. Kim, H. Cho, K. Kim, T.-W. Koh, J. Chung, J. Lee, Y. Park, S. Yoo, *Adv. Mater.* **2015**, 27, 1624.

[21] S. Reineke, F. Lindner, G. Schwartz, N. Seidler, K. Walzer, B. Lu¨ssem, K. Leo, *Nature*, **2009**, 459, 234.

[22] S. Mladenovski, K. Neyts, D. Pavicic, A. Werner, C. Rothe, *Opt. Express* **2009**, 17, 7562.

[23] Y.-H. Cheng, J.-L. Wu, C.-H. Cheng, K.-C. Syao, M.-C. M. Lee, *Appl. Phys. Lett.* **2007**, 90, 091102.

[24] S. Chen, H. S. Kwok, *Opt. Express* **2010**, 18, 37.

[25] Y.-J. Lee, S.-H. Kim, J. Huh, G.-H. Kim, Y.-H. Lee, S.-H. Cho, Y.-C. Kim, Y. R. Do, *Appl. Phys. Lett.* **2003**, 82, 3779.

[26] S. Jeon, J.-W. Kang, H.-D. Park, J.-J. Kim, J. R. Youn, J. Shim, J.-H. Jeong, D.-G. Choi, K.-D. Kim, A. O. Altun, S.-H. Kim, Y.-H. Lee, *Appl. Phys. Lett*. **2008**, 92, 223307.

[27] S. Jeon, J.-H. Jeong, Y. S. Song, W.-I. Jeong, J.-J. Kim, J. R. Youn, *Nanoscale*, **2014**, 6, 2642.

[28] S. Jeon, J.-H. Lee, J.-H. Jeong, Y. S. Song, C,-K. Moon, J.-J. Kim, J. R. Youn, *Sci. Rep.* **2015**, 5, 8865.

[29] C. Lee, J.-J. Kim, *Small*, **2013**, 9, 3858.

[30] J.-W. Shin, D.-H. Cho, J. Moon, C. W. Joo, S. K. Park, J. Lee, J.-H. Han, N. S. Cho, J. Hwang, J. W. Huh, H. Y. Chu, J.-I. Lee, *Org. Electronics*, **2014**, 15, 196.

[31] Y. Sun, S. R. Forrest, *Nat. Photonics* **2008** 2, 483.

[32] J. Choi, T.-W. Koh, S. Lee, S. Yoo, *Appl. Phys. Lett.* **2012**, 100, 233303.

[33] L. Zhou, Q.-D. Ou, Y.-Q. Li, H.-Y. Xiang, L.-H. Xu, J.-D. Chen, C. Li, S. Shen, S.-T. Lee, J.-X. Tang, *Adv. Funct. Mater.* **2015**, 25, 2660.

[34] Q.-D. Ou, L. Zhou, Y.-Q. Li, S. Shen, J.-D. Chen, C. Li, Q.-K. Wang, S.-T. Lee, J.-X. Tang, *Adv. Funct. Mater.* **2014**, 24, 7249.

[35] L. Li, J. Liang, S.-Y. Chou, X. Zhu, X. Niu, Z. Yu, Q. Pei, *Sci. Rep.* **2014**, 4, 4307.

[36] A. O. Altun, S. Jeon, J. Shim, J.-H. Jeong, D.-G. Choi, K.-D. Kim, J.-H. Choi, S.-W. Lee, E.-S. Lee, H.-D. Park, J. R. Youn, J.-J. Kim, Y.-H. Lee, J.-W. Kang, *Org. Electronics*, **2010**, 11,711.

[37] W. H. Koo, S. M. Jeong, F. Araoka, K. Ishikawa, S. Nishimura, T. Toyooka, H. Takezoe, *Nature Photon.* **2010**, 4, 222.

[38] Y.-G. Bi, J. Feng, Y.-F. Li, X.-L. Zhang, Y.-F. Liu, Y. Jin, H.-B. Sun, *Adv. Mater.* **2013**, 25, 6969.

[39] W. Youn, J. Lee, M. Xu, R. Singh, F. So, *ACS Appl. Mater. Interfaces*, **2015**, 7, 8974.

[40] C.-L. Lin, H.-W. Lin, C.-C. Wu, *Appl. Phys. Lett.* **2005**, 87 021101.

[41] C.-J. Yang, S.-H. Liu, H.-H. Hsieh, C.-C. Liu, T.-Y. Cho, C.-C. Wu, *Appl. Phys. Lett.* **2007**, 91 253508.

[42] K.-H. Kim, J.-L. Liao, S. W. Lee, B. Sim, C.-K. Moon, G.-H. Lee, H. J. Kim, Y. Chi, J.-J. Kim, *Adv. Mater.* **2016**, 28, 2526.

[43] K.-H. Kim, E. S. Ahn, J.-S. Huh, Y.-H. Kim, J.-J. Kim, *Chem. Mater.* **2016**, 28, 7505.

[44] H. Shin, J.-H. Lee, C.-K. Moon, J.-S. Huh, B. Sim, J.-J. Kim, *Adv. Mater.* **2016**, 28, 4920.

[45] J.-H. Lee, S. Lee, J.-B. Kim, J. Jang, J.-J. Kim, *J. Mater. Chem.* **2012**, 22, 15262.

[46] Y.-H. Huang, C.-Y. Lu, S.-T. Tsai, Y.-T. Tsai, C.-Y. Chen, W.-L. Tsai, C.-Y. Lin, H.-W. Chang, W.-K. Lee, M. Jiao, C.-C. Wu, *Appl. Phys. Lett.* **2014**, 104, 183302.

[47] K. Yee, *IEEE Trans. Antenn. Propag.* **1966**, 14, 302.

[48] A. Chutinan, K. Ishihara, T. Asano, M. Fujita, S. Noda, *Org. Electronics* **2005**, 6, 3.

[49] Y.-J. Lee, S.-H. Kim, G.-H. Kim, Y.-H. Lee, S.-H. Cho, Y.-W. Song, Y.-C. Kim, Y. R. Do, *Opt. Express* **2005**, 13, 5864.

[50] J. Adam, J. Hauss, S. Gleiss, B. Riedel, U. Geyer, U. Lemmer, M. Gerken, *ICTON-MW 2009. 3rd* **2009**, 1.

[51] Q. Yue, W. Li, F. Kong, K. Li, *Adv. Mater. Sci. Eng*. **2012**, 2012, 985762.

[52] J.-W. Kim, J.-H. Jang, M.-C. Oh, J.-W. Shin, D.-H. Cho, J.-H. Moon, J.-I.

Lee, *Opt. Express* **2014**, 22, 498.

[53] M. K. Callens, H. Marsman, L. Penninck, P. Peeters, H. d. Groot, J. M. t. Meulen, K. Neyts, *Opt. Express* **2014**, 22, A589.

[54] J.-G. Kim, C.-H. Hsieh, H. J. Choi, J. Gardener, B. Singh, A. Knapitsch, P. Lecoq, G. Barbastathis, *Opt. Express* **2015**, 23, 22730.

[55] J.-B. Kim, J.-H. Lee, C.-K. Moon, K.-H. Kim, J.-J. Kim, *Org. Electronics* **2015**, 17, 115.

[56] W. Wang, H. Peng, S. Wang, S. Chen, *Org. Electronics* **2015**, 24, 195.

[57] Y. Qu, C. Coburn, D. Fan, S. R. Forrest, *ACS Photonics* **2017**, 4, 363.

[58] D. Englund, D. Fattal, E. Waks, G. Solomon, B. Zhang, T. Nakaoka, Y. Arakawa, Y. Yamamoto, J. Vuc̆kovic´, *Phys. Rev. Lett.* **2005**, 95, 013904.

[59] P. T. Kristensen, C. Van Vlack, S. Hughes, *Opt. Letters* **2012**, 37, 1649.

[60] *Lumerical Solutions*, Inc. http://www.lumerical.com/tcad-products/fdtd/.

[61] R. R. Chance, A. Prock, R. Silbey, *Adv. Chem. Phys.* **1987**, 37, 1.

[62] S. Kim, J.-J. Kim, *Org, Electronics* **2010**, 11, 1010.

[63] C.-K. Moon, S.-Y. Kim, J,-H. Lee, J.-J. Kim, *Opt. Express* **2015**, 23, A279.

[64] J. D. Jackson, *John Wiley & Sons, Inc.* **1999**, 3rd edition.

[65] C.-C. Ma, Y.-J. Chen, L.-J. Hsiao, *Proc. SPIE 9137 Organic Photonics VI* **2014**, 91370J.

[66] M. C. Gather, S. Reineke, *J. Photon. Energ.* **2015**, 5, 057607.

[67] H. -W. Chang, J. Lee, S. Hofmann, Y. H. Kim, L. Müller-Meskamp, B. Lüssem, C. -C. Wu, K. Leo, M. C. Gather, *J. Appl. Phys.* **2013**, 113, 204502.

[68] H. -W. Chang, Y. H. Kim, J. Lee, S. Hofmann, B. Lüssem, L. Müller-

Meskamp, M. C. Gather, K. Leo, C. -C. Wu, *Org. Electron.* **2014**, 15, 1028.

[69] P. E. Burrows, S. R. Forrest, L. S. Sapochak, J. Schwartz, P. Fenter, T. Buma, V. S. Ban, J. L. Forrest, *J. Cryst. Growth* **1995**, 156, 91.

[70] M. Baldo, M. Deutsch, P. Burrows, H. Gossenberger, M. Gerstenberg, V. Ban,S. Forrest, *Adv. Mater.* **1998**, 10, 1505.

[71] M. A. Baldo, V. G. Kozlov, P. E. Burrows, S. R. Forrest, V. S. Ban, B. Koene, M. E. Thompson, *Appl. Phys. Lett.* **1997**, 71, 3033.

[72] S. C. Seel, C. V. Thompson, *J. Appl. Phys*. **2003**, 93, 9038.

[73] S. Lee, Orange and White Organic light Emitting Diodes using Exciplex-forming Co-hosts, PhD dissertation, Seoul National University, 2014.

[74] K.-H. Kim, C.-K. Moon, J.-H. Lee, S.-Y. Kim, J.-J. Kim, *Adv. Mater.* **2014**, 26, 3844.

[75] K.-H. Kim, S. Lee, C.-K. Moon, S.-Y. Kim, Y.-S. Park, J.-H. Lee, J. W. Lee, J. Huh, Y. You, J.-J. Kim, *Nat. Commun.* **2014**, 5, 4769.

[76] H. Shin, S. Lee, K.-H. Kim, C.-K. Moon, S.-J. Yoo, J.-H. Lee, J.-J. Kim, *Adv. Mater.* **2014**, 26, 4730.

[77] H. Sasabe, J. Takamatsu, T. Motoyama, S. Watanabe, G. Wagenblast, N. Langer, O. Molt, E. Fuchs, C. Lennartz, J. Kido, *Adv.Mater.* **2010**, 22, 5003.

[78] W. Gaynor, S. Hofmann, M. G. Christoforo, C. Sachse, S. Mehra, A. Salleo, M. D. McGehee, M. C. Gather, B. Lüssem, L. Müller-Meskamp, P. Peumans, K. Leo, *Adv. Mater.* **2013**, 23, 4006.

[79] N. Li, S. Oida, G. S. Tulevski, S.-J. Han, J. B. Hannon, D. K. Sadana, T.-C. Chen, *Nature Comm.* **2013**, 4, 2294.

[80 N. Ide, K. Yamae, V. Kittichungchit, H. Tsuji, M. Ota, T. Komoda, *J. Photopolym. Sci. Technol.* **2014**, 27, 357.

[81] K. Kato, T. Iwasaki, T. Tsujimura, *J. Photopolym. Sci. Technol.* **2015**, 28, 335.

[82] D. Riedel, T. Wehlus, T. C.G. Reusch, C. J.Brabec, *Org. Electronics*, **2016**, 32, 27.

[83] M. Du, Y. Feng, D. Zhu, T. Peng, Y. Liu, Y. Wang, M. R. Bryce, *Adv. Mater.* **2016**, 28, 5963.

[84] J. Kido, M. Kimura, K. Nagai, *Science* **1995**, 267, 1332.

[85] J. Ye, C.-J. Zheng, X.-M. Ou, X.-H. Zhang, M.-K. Fung, C.-S. Lee, *Adv. Mater.* **2012**, 24, 3410.

[86] T. Fleetham, J. Ecton, Z. Wang, N. Bakken, J. Li, *Adv. Mater.* **2013**, 25, 2573.

[87] K. Udagawa, H. Sasabe, F. Igarashi, J. Kido, *Adv. Mater.* **2016**, 4, 86.

[88] X. Zhuang, H. Zhang, K. Ye, Y. Liu, Y. Wang, *ACS Materials & Interfaces* **2016**, 8, 11221.

[89] A. R. Duggal, J. J. Shiang, C. M. Heller, D. F. Foust, *Appl. Phys. Lett.* **2002**, 80, 3470.

[90] S. Krotkus, D. Kasemann, S. Lenk, K. Leo, S. Reineke, *Light: Sci. Appl.* **2016**, 5, e16121.

[91] C.-C. Chang, J.-F. Chen, *Appl. Phys. Lett.* **2005**, 87, 253501.

[92] S. Lee, H. Shin, J.-J. Kim et al., *Adv. Mater.* **2014**, 26, 5864.

[93] H. Cho, C. W. Joo, J. Lee, H. Lee, J. Moon, J.-I. Lee, J. Y. Lee, Y. Kang, N.

S. Cho, *Opt. Express* **2016**, 24, 24161.

[94] C. Coburn, C. Jeong, S. R. Forrest, *ACS Photonics* **2017**, 10.1021.

[95] S. Lee, J.-H. Lee, J.-H. Lee, J.-J. Kim, *Adv. Funct. Mater*. **2012**, 22, 855

[96] Y.Ohno, *Energy Star Webinar March* **2016**.

[97] L. Ding, S.-C. Dong, Z.-Q. Jiang, H. Chen, L.-S. Liao, *Adv. Funct. Mater.* **2015**, 25, 645.

[98] Z. T. Zhang, S.-J. He, D.-K. Wang, N. J.iang, Z.-H. Lu, *Sci. Rep.* **2016**, 6, 20517.

[99] X.-L. Li, G. Xie, M. Liu, D. Chen, X. Cai, J. Peng, Y. Cao, S.-J. Su, *Adv. Mater.* **2016**, 28, 4614.

[100] J. M. Choi, D. R. Lee, J. Y. Lee, *Dyes and Pigments* **2017**, 142, 243.

[101] K.-H. Kim, J.-Y. Ma, C.-K. Moon, J.-H. Lee, J. Y. Baek, Y.-H. Kim, J.-J. Kim, Adv. Opt. Mater. 2015, 3, 1191.

[102] J. H. Seo, G. Y. Kim, J. H. Kim, J. S. Park, B. M. Seo, K. H. Lee, S. S. Yoon, Y. K. Kim, *J. J. Appl. Phys.* **2009**, 48, 082103.

[103] H. Lim, H. Shin, K.-H. Kim, S.-J. Yoo, J.-S. Huh, J.-J. Kim, *ACS Applied Materials & Interfaces* **2017**, 9, 37883.

초 록

유기발광소자는 최근 차세대 디스플레이 및 조명용 발광소자로 각광받고 있다. 유기발광소자가 산업계 전반에 사용되기 위해서, 광추출효율이 더욱 개선될 필요가 있다. 디스플레이용 광추출을 하기 위해서 높은 광추출효율 향상량, 시야각에 따른 낮은 스펙트럼 변화, 낮은 픽셀 빛번짐 및 높은 명암비가 요구된다. 그리고, 전면발광형 유기발광소자의 상부전극에 피해를 주지않는 공정방법이 요구된다. 조명용 광추출을 하기 위해서 높은 광추출효율 향상량, 낮은 시야각에 따른 스펙트럼 변화, 균일한 발광분포 및 높은 색품질이 요구된다. 조명은 보통 배면발광형을 사용하기 때문에 다양한 공정을 적용할 수 있지만 무기발광소자 및 다른 광원들과 경쟁해야하기 때문에 높은 광추출효율 향상량이 요구된다.

광추출효율을 향상시키기 위해서 마이크로렌즈어레이, 광결정, 산란층, 주름구조가 적용된 소자 등등 다양광 방법들이 보고되었다. 그 중, 진공증착법으로 유기물 마이크로렌즈어레이를 제작하는 방법이 제작 중 소자에 피해를 주지 않는 점과, 높은 광추출효율 향상 및 낮은 스펙트럼 변화 등의 이유로 디스플레이용 광추출구조물의 가능성을 가지고 있다. 그러나 실제 디스플레이 공정의 제조시간을 맞추기

위해서는 광추출구조물의 크기가 작아질 필요가 있다. 게다가, 구조물의 크기를 줄일 경우에는 이를 최적화하는 정교한 모델링이 필요하다. 조명용 광추출구조로선 진공홀어레이가 평탄한 표면에 의한 전기적 안정성, 반구렌즈와 함께 했을 때 높은 광추출 등의 이유로 가능성을 보인다. 육각분포의 진공나노구멍구조가 에어모드, 기판모드, 웨이브가이드모드를 전부 추출하는 보고가 있었지만, 균일한 발광분포가 필수적인 조명에서는 적용하기 힘들다는 단점이 있다.

이번 학위 논문에서는 위의 두가지 주제 (1) 디스플레이용 유기물 나노렌즈어레이가 적용된 전면발광형 유기발광소자의 광추출효율과 (2) 조명용 진공구멍어레이가 적용된 소자의 광추출효율 및 색 품질을 다룬다. 이번 논문에서 위의 두 방법이 각각 조명과 디스플레이 실용적으로 적용할 수 있는 방법임을 보일 것이다.

학위 논문은 디스플레이와 조명으로 크게 나뉘어지며, 본론에 앞서 1장에서는 유기발광소자의 효율, 광손실경로, 광추출방법 및 유한차분법에 대해 간단한 소개를 담았다.

2장에서 광추출구조가 적용된 상부발광형 유기발광소자의 광추출효율을 유한차분법으로 계산하는 방법을 담았다. 유한차분법을 사용할 때에 있어 계산 변수들의 영향에 대해서 먼저 다룬다. 최적화된 계산 변수들을 검증하기위해 고전전자기모델링으로 계산한 퍼셀인자와 광추출효율을 비교하였고, 계산 결과의 차이가 거의 없음을 확인하였다.

이를 바탕으로 유기나노렌즈어레이가 적용된 소자의 광추출효율을 계산한 결과를 정리하였다.

3장에서, 유기나노렌즈어레이로 인한 광추출효율 향상에 대해 다룬다. 임의분포를 가지는 유기나노렌즈어레이는 유기증기물리증착법을 통해 제작할 수 있다. 제작된 유기나노렌즈어레이의 구조들을 유한차분법으로 계산하여 높은 광추출효율을 가지는 분포를 제시하였다. 또한 광추출구조물이 유기물보다 더 높은 물질로 이루어질 경우에 광추출효율 향상량이 더 높아짐을 계산으로 확인하였다. 산화물인듐아연을 상부전극으로 사용한 전면발광형 소자에 유기물리증착법을 사용하여 렌즈어레이를 만들고 녹색, 청색 소자를 제작하였다. 두 소자 모두 50%이상의 광추출효율 향상량을 보였으며, 계산에서 얻은 향상량과 일치했다.

4장에선, 진공나노구멍구조를 임의적으로 분포시킨 후 백색 유기발광소자에 적용한 것에 대해 다룬다. 이때 외부양자효율은 78%, 전력효율은 164 lm/W라는 현재까지 보고된 값 중 가장 높은 값을 가지는 결과이다. 임의분포를 형성하기 위해 반지름이 각각 120, 150, 190 nm인 나노홀을 임의숫자생성함수를 사용하여 분포시켰다. 기판의 바깥쪽에 반구렌즈를 적용하여 공기, 기판, 웨이브가이드 모드를 전부 추출할 수 있었다. 임의분포 덕분에 백색 소자의 시야각에 따른 스펙트럼 변화는 거의 없었고, 균일한 발광 패턴을 가지는 소자가

제작되었다. Si_3N_4와 공기로 이루어진 광추출 구조물의 높은 광추출효율 향상량의 기원을 파악하기 위해 FDTD 계산을 하였다. 유전층과 nano hole array의 굴절률 차이가 클수록, 광추출 효율이 크며 내부에 waveguide가 거의 추출되는 것을 알 수 있었다.

5장에서 다양한 광추출구조가 적용되었을 때 이론적으로 얻을 수 있는 탠덤 백색소자의 색 품질에 대해 다룬다. 먼저 염료들의 비율에 따른 PL 스펙트럼 합이 가지는 색 품질을 계산하여 색 좌표에 따른 연색성을 계산하였다. 다음으로 마이크로 공진구조를 감안하여, 광추출구조가 없는 소자, 반구렌즈가 적용된 소자, 고굴절 기판과 고굴절 반구렌즈가 적용된 소자 및 고굴절 기판과 고굴절 반구렌즈와 두꺼운 전자수송층이 적용된 소자가 가지는 색 품질을 계산하였다. 마이크로 공진구조가 강할수록 청색 염료의 두번째 픽의 크기가 감소하고, PL로 얻을 수 있는 최종 색 품질과의 차이가 커지는 것을 발견했다. 모델링에 대한 검증을 위해 고효율 탠덤 백색소자를 제작하여 반구렌즈 유무에 따른 스펙트럼을 비교하였고, 스펙트럼 비율을 잘 추적하는 것을 확인하였다. 이때 제작된 소자는 6500 K 이상의 높은 색온도를 가지며 38 lm/W의 전력 효율 및 80 이상의 연색성을 가지는 고품질 소자가 구현되었다.

주요어: 유기발광소자, 광추출, 상부발광형 유기발광소자,

유기발광소자 조명, 유한차분법, 몬테-칼로, 주기격자이론

학번: 2013-30767

CURRICULUM VITAE

Kyung-Hoon Han

Department of Materials Science and Engineering

Seoul National University, Seoul, 151-744, Korea

+82-2-875-2412 (Office)

E-mail: gogoorc@snu.ac.kr

Education

2013.03 ~ 2018.02 **Ph.D.** in Materials Science and Engineering
Supervisor: Professor Jang-Joo Kim
Seoul National University, Seoul, Korea

2011.03 ~ 2013.02 **M.S.** in Materials Science and Engineering
Supervisor: Professor Jang-Joo Kim
Seoul National University, Seoul, Korea

2007.03 ~ 2011.02 **B.S.** in Materials Science and Engineering
Seoul National University, Seoul, Korea

Research Interests

Organic light-emitting diodes, light extraction efficiency, finite difference time domain method, display, lighting, color quality, computational electromagnetics

Professional Skills

- Design and fabrication of organic electronic devices: Thermal evaporator, Glove-box, Spin coater

- The optoelectronic analyses on organic semiconductors: UV-vis-NIR absorption spectroscopy, OLEDs characteristic measurements, Angle dependent EL analysis
- The structural characterization of organic semiconductors: AFM, α-STEP
- Finite difference time domain calculations
- Rigorous coupled wave analysis calculations
- Ray tracing calculations

Scholarship and Fellowship

- Brain Korea 21 Scholarship (2011.03~)
- World Class University (WCU) project through National Research Foundation of Korea funded by the Ministry of Education, Science and Technology (2011.03~)

List of Publications

1. Yang Doo Kim(+), Kyung-Hoon Han(+), Sang-Jun Park, Jung-Bum Kim, Ju-Hyeon Shin, Jang Joo Kim, and Heon Lee, "Enhanced light extraction efficiency in organic light emitting diodes using a tetragonal photonic crystal with hydrogen silsesquioxane", *Opt. Lett.* **2014**, 39, 5901.

2. Yang Doo Kim(+), Kyung-Hoon Han(+), Young Hoon Sung, Jung-Bum Kim, Hak-Jong Choi, Heon Lee, Jang-Joo Kim, "Enhanced light extraction efficiency in organic light-emitting diode with randomly dispersed nanopattern", *Opt. Lett.* **2015**, 40, 5838.

3. Cholho Lee, Kyung-Hoon Han, Kwon-Hyeon Kim, Jang-Joo Kim, "Direct formation of nano-pillar arrays by phase separation of polymer blend for the enhanced out-coupling of organic light emitting diodes with low pixel blurring", *Opt. Express* **2016**, 24, A488.

4. Young-Sam Park(+), Kyung-Hoon Han(+), Jehan Kim, Doo-Hee Cho, Jonghee Lee, Yoonjay Han, Jong Tae Lim, Nam Sung Cho, Byounggon Yu, Jeong-Ik Lee, Jang-Joo Kim, "Crystallization-assisted nano lens array fabrication for highly efficient and color stable organic light emitting diodes", *Nanoscale* **2017**, 9, 230.

5. Young Hoon Sung(+), Pil-Hoon Jung(+), Kyung-Hoon Han, Yang Doo Kim, Jang-Joo Kim, Heon Lee, "Improved out-coupling efficiency of organic light

emitting diodes fabricated on a TiO2 planarization layer with embedded Si oxide nanostructures", *Optical Materials* **2017**, 72, 828.

6. Young Hoon Sung, Kyung-Hoon Han, Yang Doo Kim, Yoonjay Han, Jang-Joo Kim, Heon Lee, "Air void optical scattering structure for high-brightness organic light emitting diodes", *Ceramics International* **2017**, 43, S455.

List of Presentations

International Conference

1. **Kyung-Hoon Han**, Yang-Doo Kim, Young-Hoon Sung, Jung-Bum Kim, Hak-Jong Choi, Heon Lee, Jang-Joo Kim, "Enhanced Light Extraction Efficiency in Organic Light-emitting Diode with Randomly Dispersed Nanopattern", A-COE2015, October 29-31 (October 30), 2015, China (Poster)
2. **Kyung-Hoon Han**, Yang-Doo Kim, Young-Hoon Sung, Jung-Bum Kim, Hak-Jong Choi, Heon Lee, Jang-Joo Kim, "Enhanced light extraction efficiency in organic light-emitting diode with randomly dispersed nanopattern", The 7th International Workshop on Flexible & Printable Electronics 2015 (IWFPE 2015), November 4-6 (November 5), 2015, Korea (Poster)
3. Cholho Lee, **Kyung-Hoon Han**, Kwon-Hyeon Kim, Jang-Joo Kim, "Direct formation of nano-pillar arrays by phase separation of polymer blend for the enhanced out-coupling of organic light emitting diodes with low pixel blurring", The International Symposium on Recent Advanes and Future Issues in Organic Electroluminscence (ISOEL2016), February 17-19 (February 18), 2016, Korea (Poster)
4. Young-Sam Park, **Kyung-Hoon Han**, Doo-Hee Cho, Jonghee Lee, Yoon-Jay Han, Nam Sung Cho, Byoung-Gon Yu, Jang-Joo Kim, Jeong-Ik Lee, "Maskless Integration of Nano Lens Arrays (NLAs) on Inverted Top Emitting Organic Light Emitting Diodes (TEOLEDs) for High Light Extraction

Efficiency", OSA Light, Energy & Environment Congress, November 14-17 (November 16), 2016, Germany (Poster)

5. Sohee Jeon, Sunghun Lee, **Kyung-Hoon Han**, Hyun Shin, Kwon-Hyeon Kim, Jun-Ho Jeong, Jang-Joo Kim, "High Quality White OLEDs with Comparable Efficiencies to LEDs using randomly dispersed vacuum nanohole array", The 28th Internaional Conference on Molecular Electronics and Devices 2017 (IC ME&D 2017), May 18-19 (May 18), 2017, Korea (Poster)
6. **Kyung-Hoon Han**, Sohee Jeon, Sunghun Lee, Kwon-Hyeon Kim, Hyun Shin, Jun-Ho Jeong, Jang-Joo Kim, "High quality white OLEDs with LED efficiencies", SPIE Optics+Photonics 2017, August 6-10 (August 6), 2017, USA (Poster)
7. Young-Sam Park, **Kyung-Hoon Han**, Doo-Hee Cho, Jehan Kim, Byouggon Yu, Nam Sung Cho, Jang-Joo Kim, Jeong-Ik Lee, "A Nano-lens Array Fabrication Using a Mask-free Deposition for Highly Efficient and Pixel Blur-free Top-emitting OLEDs", The 17th International Meeting on Information Display (iMiD 2017), August 28-31 (August 31), 2017, Korea (Oral)
8. Sohee Jeon, Sunghun Lee, **Kyung-Hoon Han**, Hyun Shin, Kwon-Hyeon Kim, Jun-Ho Jeong, Jang-Joo Kim, "Optical Analysis of White Organic Light Emitting Diodes with Randomly Dispersed Nano-pillar Array", The 17th International Meeting on Information Display (iMiD 2017), August 28-31 (August 31), 2017, Korea (Poster)

Domestic Conference

1. **한경훈**, 김장주, "Enhanced light extraction efficiency of organic light emitting diodes using hydrogen silsesquoxane nano-pillar arrays", 2013 한국고분자학회 춘계학술대회, April 11-12, 2013 (Poster)
2. **한경훈**, 이철호, 김장주, "The Enhanced Out-Coupling of Organic Light Emitting Diodes with Low Haze using Nano Pillar Arrays Directly Formed by Phase Separation of Polymer Blend", 2014 Materials Fair, September 25, 2014, Korea (Poster)
3. **한경훈**, 김장주, "Direct formation of nano-pillar arrays by phase separation of polymer blend for the enhanced out-coupling of organic light emitting diodes with low pixel blurring", 2016 한국고분자학회 춘계학술대회, April 6-8 (April 8), 2016, Korea (Poster)